Report no. changed (Mar 2006): SR-292-UU

SACLANTCEN REPORT
serial no: SR-292

SACLANT UNDERSEA RESEARCH CENTRE REPORT

NOWCASTING AND FORECASTING OF SOUND VELOCITY STRUCTURE BY OCEAN MODELLING

R. Onken

April 1999

SACLANT Undersea Research Centre
Viale San Bartolomeo 400
19138 San Bartolomeo (SP), Italy

tel: +39-0187-5271
fax: +39-0187-524.600

e-mail: library@saclantc.nato.int

NORTH ATLANTIC TREATY ORGANIZATION

Report no. changed (Mar 2006): SR-292-UU

Nowcasting and forecasting of sound velocity structure by ocean modeling

Reiner Onken

The content of this document pertains to work performed under Project 022-3 of the SACLANTCEN Programme of Work. The document has been approved for release by The Director, SACLANTCEN.

Jan L. Spoelstra
Director

intentionally blank page

Nowcasting and forecasting of sound velocity structure by ocean modeling

Reiner Onken

Executive Summary: Because of its impact on underwater detection, the spatial distribution of sound velocity in the ocean and its time variability is of main interest in military oceanography. As an alternative to climatological mean conditions, oceanographic models are used for the extension in space and time of sparse measurements of the sound velocity profile. For the case of a varying environment in the Eastern Mediterranean Sea, it is demonstrated that the description of the present and predicted sound velocity structure by a dynamic ocean model is superior to climatology and to simple data interpolation schemes. For this study, part of survey data are assimilated into the model with the temporal and spatial scales of sound velocity variability taken into account which are imposed by ocean dynamics. The rest of survey data is used for validation of the model results.

Report no. changed (Mar 2006): SR-292-UU

intentionally blank page

Nowcasting and forecasting of sound velocity structure by ocean modeling

Reiner Onken

Abstract: The Harvard Ocean Prediction System (HOPS) is applied to an observed oceanographic data set in order to demonstrate that a dynamical ocean model is able to provide meaningful extensions in space (nowcast) and time (forecast) of the sound velocity field. The model is set up with a high number of vertical layers in order to resolve sufficiently the details of sound velocity profiles. The high resolution observational data collected in February 1997 in the Antalya Basin (Eastern Mediterranean Sea) is serving for initialization of the model and for validation of the model results.

For assessing the nowcast capability, HOPS is initialized by a subset of observational data at half the horizontal resolution of the original sampling scheme. The sound velocity field is obtained by objective analysis. Observations are weighted by a correlation function that uses the Rossby radius as a natural scale of influence for dynamical processes in the ocean. The modelled sound velocity distribution is validated by comparison with the full resolution observed distribution at the respective locations, and it is shown that the objectively analyzed sound velocity matches the observations better than the sound velocity distribution obtained by a classical interpolation scheme with inverse distance weighting.

For the forecast experiment, the observational data set is separated in two subsets which occupy the same positions but are different in time. HOPS is initialized with the earlier data set and integrated in time until the end of the survey. By comparing the forecasted and observed sound velocity during the course of the integration, it is verified that the predicted profiles, their vertical gradients, and the depth of the main sound channel axis provide a better match with the validation data than making the assumption that no change has occurred during the forecast period.

Keywords: eastern Mediterranean ○ sound velocity ○ nowcast ○ forecast ○ ocean modeling

Contents

List of Figures

1
Introduction

A primary objective of military oceanography is to determine the conditions for target localisation by underwater sound. Sound waves in the ocean are affected by reflection, scattering, refraction and absorption. These processes act in the water column (volume scattering, absorption, refraction), at the air-sea and bottom interfaces (reflection, scattering), or in the bottom halfspace (absorption). The importance of the different processes depends on the frequency of sound waves and on the situation under consideration, such as shallow or deep water. Bottom scattering and absorption are due to permanent properties of a specific area. Interactions with the rough ocean surface depend on the actual weather condition which is easy to observe. In the water column, sound propagation conditions are controlled by volume absorption and scattering due to marine life, predictive models of which will be available one day as a result of present interdisciplinary effort, and by the sound speed structure which is a function of the physical parameters temperature, salinity and pressure only. In the following investigation, only the predictability of the internal sound velocity field is taken into consideration.

The most common method to predict for an ocean area sound velocity as function of depth, is by selection of a representative profile from a historical data base. An appropriate profile must belong to the pertinent season. It will either be an instance of archived measurements or the average of measurements. For the purpose of sound propagation calculations, there is no indisputable preference for smoothed climatology against single historical profiles. Obviously, sound velocities from a historical data base do not reflect the response of the ocean to the actual weather situation and the current status of varying mesoscale ocean features. Predictions of sound velocity profiles from climatology are usually not accompanied with confidence intervals. Approximate scales for spatial variations are never given.

As soon as it is possible to measure sound velocity in the ocean area of interest, predictions are replaced by measurements. Expendable instruments can be used without affecting ship operations. On their way down to the ocean bottom, they transmit measurement values through a thin copper wire that finally breaks. Below a few hundred meter water depth, deviations of the sound velocity from climatological values are small and may be neglected. Instead of expendable sound velocity meters (XSV), usually much less expensive bathythermographs (XBT) are deployed. In most ocean areas, the sound velocity profile can be calculated with sufficient accuracy from a measured temperature profile and a mean historical salinity profile. Where the combination of actual and historical data seems to be inadequate, instead of an XSV a dual parameter instrument (XCTD) is preferrable. Not only sound velocity can be calculated from the measured profiles of temperature and salinity, but also density. An unstable density profile would be an indication for a measurement problem. The other way around, even unfamiliar looking temperature or sound velocity profiles become trustworthy if they are supported by a steady and stable density profile.

Horizontal changes of the sound velocity field are obtained by repeated observations in a sampling scheme. As the required spacing is closely linked to the dynamical scales of ocean motions, i.e. the horizontal scales of fronts and eddies, it is vital to have some knowledge on these scales for the specific area of interest. In many situations a description of the status quo (a *nowcast*) of the three-dimensional sound velocity structure is not sufficient. It is desirable to have an imagination on how the sound velocity distribution will change in future - there is need for a *forecast*. The period for which a forecast is required depends on the task to be accomplished and on the time scales of environmental dynamics and may vary from hours over days to weeks or more.

Ocean modeling is a potential tool for nowcasting and forecasting the structure of sound velocity in a specific area. The capabilities for nowcasting involve making estimates on the shape of sound velocity profiles in undersampled regions which are consistent with the dynamical background. This is possible, if the predominant horizontal scales of oceanic motions are known. Forcasting involves the prediction of the evolution of sound velocity structure, which is driven by temporal changes of the temperature and salinity fields. It is accomplished by solving numerically the differential equations which describe the thermodynamics of seawater and fluid motions in geophysical systems. In the present paper, it will be demonstrated how a specific ocean model, the Harvard Ocean Prediction System (HOPS), can improve nowcasts and provide meaningful forecasts of sound velocity structure. A hydrographic data set collected in winter 1997 in the Eastern Mediterranean will be used for initialization of HOPS and for validation of the model products.

The paper is organized as follows: Some basic knowledge, which is necessary to understand how an ocean model works, is conveyed in Section 2. This section may be skipped by readers familiar with that subject. The hydrographic data set is presented in Section 3 and the HOPS model domain and grid setup is described in Section 4. Section 5 demonstrates the need of sound velocity measurements by comparison of actually measured profiles with those obtained from climatology. The nowcasting capabilities of HOPS are presented in Section 6, and in Section 7 it will be shown how HOPS can be utilized for forecasting the sound velocity structure. Section 8 contains the conclusions.

2

Fundamentals of ocean modeling

This section covers some basic aspects of ocean modeling. The matter presented in Subsections 2.1, 2.2, and 2.3.1 is elementary and may be found in any textbook of ocean dynamics, for example [1], [2], or [3]. For additional information on procedures for numerical solutions (Subsection 2.3.2), the reader is referred to [4] or [5], and more details on data assimilation techniques (Subsection 2.4) are found in [6].

2.1 The system of equations for a material element of seawater

The physical state of the ocean can be completely described, if the basic quantities temperature (T), salinity (S), pressure (p), density (ϱ) and the zonal, meridional, and vertical velocity components of the velocity vector $\mathbf{U} = (u, v, w)$ (bold face letters denote vector quantities) are known at every location in three-dimensional space. In that case, any other physical quantity, except for those depending on organic components, can be expressed in terms of the basic quantities.

A major objective of physical oceanography is to formulate laws in the form of mathematical equations which describe temporal changes of the basic quantities. These laws are based on axioms of physics expressing the conservation of momentum, mass, and internal energy.

Conservation of momentum is expressed by the *momentum equation*, which is applied in the form of Newton's second law. It states that the acceleration $d\mathbf{U}/dt$ (i. e. the infinitesimal rate of change of velocity $\mathbf{U}$ within an infinitesimal period of time dt) of a material element of water is proportional to the resulting force $\mathbf{F}$ and inverse proportinal to its mass M. In the ocean, the resulting force $\mathbf{F}$ is the sum of the single forces $\mathbf{F}_c$, $\mathbf{F}_p$, $\mathbf{F}_g$, $\mathbf{F}_f$, and $\mathbf{F}_t$, which are the Coriolis force due to the earth's rotation, the pressure gradient force caused by spatial pressure differences, the gravitational force, friction and tidal forces. Hence, the momentum equation reads

$$\frac{d\mathbf{U}}{dt} = \frac{1}{M}(\mathbf{F}_p + \mathbf{F}_c + \mathbf{F}_g + \mathbf{F}_f + \mathbf{F}_t). \qquad (1)$$

The *continuity equation* describes conservation of mass. It states that the rate of change of the density ϱ of a material element is balanced by the divergence of the velocity field $div(\mathbf{U})$,

$$\frac{d\varrho}{dt} = \varrho\ div(\mathbf{U}). \tag{2}$$

Here, $div(\mathbf{U})$ is the rate of change of the volume of the element due to net compression/expansion caused by different velocities at its sidewalls.

A special formulation of the mass conservation equation applied to the mass of salt contained in seawater describes the rate of change of salinity S,

$$\frac{dS}{dt} = D_S, \tag{3}$$

where D_S is the net gain of salt due to diffusion across the sidewalls of the material element. Note that a divergent flow field (as in the continuity equation above) does not alter its salinity, because salinity is defined as the ratio of the mass of salt and the mass of seawater, which remains constant in case of compression/expansion.

Internal energy is the total amount of energy of a material element of seawater except for kinetic energy due to the motion of the element, potential energy due to its vertical position in the gravity field of the earth, and chemical energy. In this special case, the internal energy can completely be described by the temperature T. According to the first law of thermodynamics, the rate of change of temperature is balanced by diffusive transport of heat (D_T) across the sidewalls, the work done by pressure (P_T) acting on the element, and internal heating due to the absorption of solar radiation (R_T) inside the element. The *heat equation* then reads

$$\frac{dT}{dt} = D_T + P_T + R_T. \tag{4}$$

An additional equation, the *equation of state*,

$$\varrho = \varrho(S, T, p) \tag{5}$$

is needed for describing the relationship between density, temperature, salinity, and pressure.

Equations (1)–(5) form a set of seven differential equations (note that (1) is a vector equation composed of three scalar equations) which is necessary for solving of the seven unknown basic quantities. As these equations describe the physics of the ocean only in its interior, they have to be replaced by *boundary conditions* at the seabed, the sea surface, and lateral boundaries, taking account of the special physical conditions at these locations. The general formulation of the boundary conditions is rather complicated. Therefore, in the following only the physical processes at the boundaries will be discussed. The momentum equations (1) must contain additional terms describing the momentum change due to interaction with the boundaries. At the seabed and at the coast, momentum is destroyed by friction, hence extra frictional terms have to be added. A gain of momentum occurs at the sea surface due to atmospheric winds. The continuity equation (2) has to be re-formulated in the way that no velocities normal to the boundaries can occur, except for the ocean-atmosphere interface where the vertical velocity is equal to the rate of change of the interface position. Extra terms taking account of salinity changes due to precipitation and evaporation have to be added to equation (3). Finally, terms describing the effects of cooling and heating due to fluxes of latent and sensible heat and radiation at the sea surface have to be added to the heat equation (4).

2.2 The system of equations for temporal changes at a fixed location

Equations (1)–(4) contain the time t as independent variable — they are *prognostic* equations, which means that any solution provides a prediction of the future evolution of the ocean. However, the problem is that (1)–(4) describe the evolution of the physical properties of a *material* element of seawater. In order to obtain a solution for a specific geographic area, it would be necessary to solve the equations individually for *every* material element of seawater residing in the area and also for those which may drift into it. Regardless of the question whether this is feasible, one is generally not interested in tracking the history of individual water particles. Instead, it is desirable to obtain solutions which describe the temporal evolution of the physical properties at a *fixed location*. To achieve that, the differential operator d/dt is substituted by a sum of differential expressions, which reads for any physical property X

$$\frac{dX}{dt} \equiv \frac{\partial X}{\partial t} + u\frac{\partial X}{\partial x} + v\frac{\partial X}{\partial y} + w\frac{\partial X}{\partial z}, \tag{6}$$

where x, y, z are the Cartesian coordinate axes directed towards east, north, and upwards, respectively. Applying (6) to (1) yields the so-called *primitive equations*

$$\begin{aligned}
\frac{\partial u}{\partial t} &= -\left(u\frac{\partial u}{\partial x} + v\frac{\partial u}{\partial y} + w\frac{\partial u}{\partial z}\right) + \frac{1}{\varrho}\left(\mathbf{F}_c^x + \mathbf{F}_p^x + \mathbf{F}_f^x + \mathbf{F}_t^x\right) && (7)\\
\frac{\partial v}{\partial t} &= -\left(u\frac{\partial v}{\partial x} + v\frac{\partial v}{\partial y} + w\frac{\partial v}{\partial z}\right) + \frac{1}{\varrho}\left(\mathbf{F}_c^y + \mathbf{F}_p^y + \mathbf{F}_f^y + \mathbf{F}_t^y\right) && (8)\\
\frac{\partial w}{\partial t} &= -\left(u\frac{\partial w}{\partial x} + v\frac{\partial w}{\partial y} + w\frac{\partial w}{\partial z}\right) + \frac{1}{\varrho}\left(\mathbf{F}_c^z + \mathbf{F}_p^z + \mathbf{F}_g^z + \mathbf{F}_f^z + \mathbf{F}_t^z\right) && (9)
\end{aligned}$$

for the three components of the momentum equation (1), where the superscripts x, y, and z denote the Cartesian components of the forces defined above. As the horizontal components of the gravitational force are zero, they have been dropped in (7) and (8). In addition, division of the equation by the volume has replaced the mass M by the density ϱ. The continuity equation (2) reads

$$\frac{\partial \varrho}{\partial t} = -\left(u\frac{\partial \varrho}{\partial x} + v\frac{\partial \varrho}{\partial y} + w\frac{\partial \varrho}{\partial z}\right) + \varrho\left(\frac{\partial u}{\partial x} + \frac{\partial v}{\partial y} + \frac{\partial w}{\partial z}\right), \tag{10}$$

where $div(\mathbf{U})$ was replaced by the equivalent differential expression. Finally, (3) and (4) describing salinity and temperature changes are written as

$$\frac{\partial S}{\partial t} = -\left(u\frac{\partial S}{\partial x} + v\frac{\partial S}{\partial y} + w\frac{\partial S}{\partial z}\right) + D_S \tag{11}$$

$$\frac{\partial T}{\partial t} = -\left(u\frac{\partial T}{\partial x} + v\frac{\partial T}{\partial y} + w\frac{\partial T}{\partial z}\right) + D_T + P_T + R_T. \tag{12}$$

Equations (7)–(12) (together with (5), which remains unchanged) are forming a set of equations for the the temporal change of the basic quantities u, v, w, ϱ, S, and T at a fixed position (the left hand side of the equations). The first term in parenthesis on the right hand side describes the advection of the respective property by the three-dimensional velocity field, and the other terms have the same meaning as in (1)–(4). For example, the temporal change of temperature at a fixed position ($\partial T/\partial t$ in (12)) is controlled by $u \cdot \partial T/\partial x$, which is the west–east advection (u) of west–east temperature gradients ($\partial T/\partial x$), by the equivalent process in north–south ($v \cdot \partial T/\partial y$) and vertical ($w \cdot \partial T/\partial z$) direction, and by diffusion of heat, pressure work, and solar heating as described above.

2.3 *How to obtain solutions*

The above equations provide a full description of the posed problem, however, there is a major problem — the equations are nonlinear, and there is no general theory available for analytical solutions of nonlinear partial differential equations. The nonlinearities are located in the first term in parenthesis on the right hand side of (7)–(12) containing products of the independent variables and their derivatives. In order to obtain solutions anyway, two approaches are common. The first is to simplify the equations in a way that they can be solved analytically for a special situation. An important and widely used product of this approach is the *geostrophic balance* and its solution, the *geostrophic currents*. These will be discussed below, because they are also relevant for ocean modeling. The second approach is to seek *numerical solutions*.

2.3.1 *Geostrophic currents*

A special situation leading to a simple solution is depicted by the following assumptions:

- We are confined to the interior of the ocean, i. e. far away from coastal boundaries, the sea surface and the seabed. Therefore, it can be assumed that the impact of frictional forces on oceanic motions is considerably smaller than the other forces and may be neclected, hence $\mathbf{F}_f^x = \mathbf{F}_f^y = \mathbf{F}_f^z = 0$.

- We are interested only in horizontal flow patterns, hence all terms containing the vertical velocity w or its derivatives, may be dropped.
- We are interested only in the time-invariant (stationary) part of the flow, hence all time derivatives $\partial/\partial t = 0$ and also the tidal force may be dropped: $\mathbf{F}_t^x = \mathbf{F}_t^y = \mathbf{F}_t^z = 0$.

If these assumptions are met, it can be shown that the magnitude of the remaining nonlinear terms is significantly smaller than the magnitude of the other forces, and may be dropped as well. In the same way, the vertical component of the Coriolis force, $\mathbf{F}_c^z$, can be neglegted when compared to the gravitational force. The momentum equation (7)–(9) then reads

$$
\begin{aligned}
0 &= \mathbf{F}_c^x + \mathbf{F}_p^x && (13)\\
0 &= \mathbf{F}_c^y + \mathbf{F}_p^y && (14)\\
0 &= \qquad \mathbf{F}_p^z + \mathbf{F}_g^z. && (15)
\end{aligned}
$$

Obviously, the pressure gradient force and the Coriolis force balence each other in the horizontal direction, whereas in the vertical direction the pressure gradient force is balanced by the gravitational force. The meaning of these balances for the horizontal flow field becomes evident after substituting the full mathematical expressions

$$
\begin{array}{lll}
\mathbf{F}_c^x = -fv & \mathbf{F}_p^x = -\dfrac{1}{\varrho}\dfrac{\partial p}{\partial x} & \\
\mathbf{F}_c^y = \quad fu & \mathbf{F}_p^y = -\dfrac{1}{\varrho}\dfrac{\partial p}{\partial y} & \\
 & \mathbf{F}_p^z = -\dfrac{1}{\varrho}\dfrac{\partial p}{\partial z} & \mathbf{F}_g^z = -g
\end{array}
$$

for the components of the forces. Here, g=9.81 ms^{-2} is the acceleration due to gravity, $\partial p/\partial x$, $\partial p/\partial y$, and $\partial p/\partial z$ the pressure change in the three coordinate directions, and $f = 2\Omega\ sin\varphi$ the *Coriolis parameter* with $\Omega = 7.292 \cdot 10^{-5}\text{s}^{-1}$ being the angular velocity of the earth and φ the geographical latitude. Then, (13)–(15) become after some re-arranging

$$
\begin{aligned}
v &= -\frac{1}{\varrho f}\frac{\partial p}{\partial x} && (16)\\
u &= \frac{1}{\varrho f}\frac{\partial p}{\partial y} && (17)\\
g &= -\frac{1}{\varrho}\frac{\partial p}{\partial z}. && (18)
\end{aligned}
$$

(16) and (17) are forming the geostrophic balance relating the horizontal components of the flow, the geostrophic currents, u and v, to the horizontal pressure gradients. Note that the east component, u, is balanced by the north–south pressure gradient

$\partial p/\partial y$ and the north component, v, by the east-west pressure gradient $\partial p/\partial x$ in a way that (on the northern hemisphere where f is positive) high pressure is always on the right when looking downstream. Hence, low pressure regions are accompanied by counter-clockwise (cyclonic) and regions of high pressure by clockwise (anticyclonic) horizontal flow.

At the first glance, the geostrophic relationship appears to be easily applicable for practical use. As ϱ is a known function of S, T, and p according to (5), and f is constant for a given latitude, it would only be necessary to measure the distribution of salinity, temperature and pressure in the ocean (for example by CTD), and then calculate u and v. But there arises a serious problem — the pressure gradient terms, $\partial p/\partial x$ and $\partial p/\partial y$, denote the change of pressure along a horizontal *level* surface, that is a surface of constant gravitational potential. As the position of these surfaces is not known sufficiently (i. e. in the ocean it is not clear what "horizontal" means), it is impossible to calculate pressure gradients with the required accuracy. One might argue that the sea surface could be used as level surface, however, the sea surface itself is distorted by geostrophic currents and is generally not horizontal. Therefore, it is common practise to postulate that there exists a depth, a *level of no motion*, where the pressure surfaces are horizontal and the geostrophic velocity is zero. The geostrophic velocities are then proportional to the horizontal gradient of the vertically integrated specific volume anomaly, which is equivalent to evaluating the horizontal pressure gradients relative to this level.

2.3.2 *Numerical solutions*

The only way to solve the set of differential equations (7)–(12) without making any simplifying assumptions is by seeking numerical solutions, which in most cases is performed using the *grid point method*. This methods makes use of the fact that any function $F(\xi)$ (where ξ is an arbitrary independent variable) can be expanded in an infinite *Taylor series* at any location $\xi = \xi_0$,

$$F(\xi_0 + \Delta\xi) = F(\xi_0) + \frac{dF(\xi_0)}{d\xi}\Delta\xi + \frac{1}{2!}\frac{d^2F(\xi_0)}{d\xi^2}(\Delta\xi)^2 + \frac{1}{3!}\frac{d^3F(\xi_0)}{d\xi^3}(\Delta\xi)^3 + \cdots, \quad (19)$$

where $\Delta\xi$ means a finite interval of the variable ξ, $2! = 1 \cdot 2$, and $3! = 1 \cdot 2 \cdot 3$. Thus, the first derivative at $\xi = \xi_0$ can be written as *finite difference equation*

$$\frac{dF(\xi_0)}{d\xi} = \frac{F(\xi_0 + \Delta\xi) - F(\xi_0)}{\Delta\xi} - R^{(2)} \quad (20)$$

with $R^{(2)}$ being the remainder of the Taylor series containing second and higher order derivatives. To demonstrate in an example how this algorithm can be used for solving a differential equation, it will be applied to the heat equation (12) at a fixed location ($x = x_0, y = y_0, z = z_0$) in space at time $t = t_0$. For simplicity, the terms D_T, P_T, R_T are omitted and the remainder of the Taylor series as well.

$$\frac{T(t_0+\Delta t)-T(t_0)}{\Delta t} \approx \tag{21}$$
$$-\left[u\frac{T(x_0+\Delta x)-T(x_0)}{\Delta x}+v\frac{T(y_0+\Delta y)-T(y_0)}{\Delta y}+w\frac{T(z_0+\Delta z)-T(z_0)}{\Delta z}\right].$$

Solving (21) for $T(t_0 + \Delta t)$ yields

$$T(t_0+\Delta t) \approx T(t_0) \tag{22}$$
$$-\Delta t\left[u\frac{T(x_0+\Delta x)-T(x_0)}{\Delta x}+v\frac{T(y_0+\Delta y)-T(y_0)}{\Delta y}+w\frac{T(z_0+\Delta z)-T(z_0)}{\Delta z}\right],$$

hence, if $T(t_0)$ represents the *actual* temperature, the finite difference formulation enables a forecast for $t = t_0 + \Delta t$ based on the actual flow field (u, v, w) and the actual temperature gradients. Note that the Taylor series expansion in (19) and (20) is an exact relationship, whereas (21), (22) are approximate solutions, because the remainders of the Taylor series were dropped. In this case, the *truncation error* of the finite difference equation is of second order, because the Taylor series was truncated after the first derivative. By taking account of the higher order terms, the truncation error may be reduced.

Equation (22) provides a solution only for the time $t = t_0 + \Delta t$ at the position (x_0, y_0, z_0). In order to obtain solutions everywhere, a three-dimensional grid is defined on the geographical area of interest, separating the *model domain* into a finite number of (not necessarily equally-spaced) *grid cells* (Figure 1). Each cell has the widths Δx, Δy, Δz in x, y, and z-direction, respectively. The dependent variables (in this case u, v, w, and T) are defined in every cell and (22) is then solved for every cell independently. If the model domain is divided in

I grid intervals $(1, 2, 3, \cdots, i-1, i, i+1, \cdots, I)$ in x-direction
J grid intervals $(1, 2, 3, \cdots, j-1, j, j+1, \cdots, J)$ in y-direction and
K grid intervals $(1, 2, 3, \cdots, k-1, k, k+1, \cdots, K)$ in z-direction,

then every cell may be identified by the triple subscript (i, j, k), and (22), written as

$$T^{n+1}_{i,j,k} \approx T^n_{i,j,k} \tag{23}$$
$$-\Delta t\left[u^n_{i,j,k}\frac{T^n_{i+1,j,k}-T^n_{i,j,k}}{\Delta x}+v^n_{i,j,k}\frac{T^n_{i,j+1,k}-T^n_{i,j,k}}{\Delta y}+w^n_{i,j,k}\frac{T^n_{i,j,k+1}-T^n_{i,j,k}}{\Delta z}\right],$$

has to be solved for all combinations of i, j, and k, where the superscript n denotes the actual and $n+1$ the future time level.

In principle, the grid increments Δx, Δy, and Δz, may be selected arbitrarily depending on the spatial resolution wanted by the modeler. In contrast, there exists

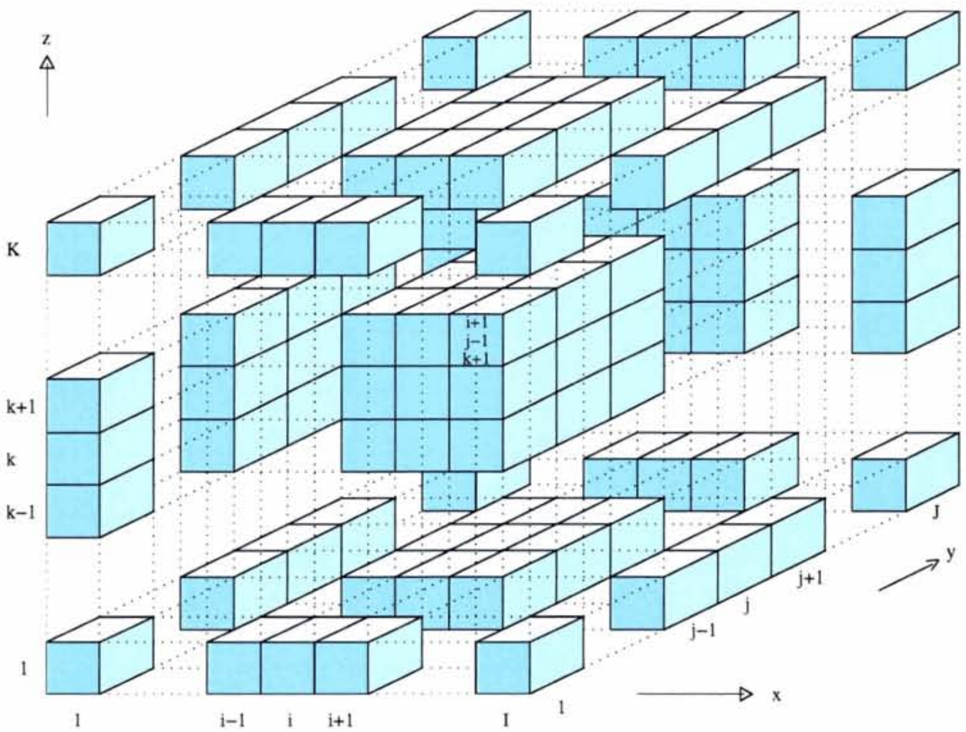

Figure 1 *Arrangement of grid cells in a numerical grid. The number of grid cells in x, y, and z direction is I, J, and K, respectively. Only a fraction of the cells is shown. The triple $(i+1, j-1, k+1)$ of the cell in the central block is an example for a cell address.*

an upper bound for the time interval Δt depending on the choice of the spatial grid increments and on the magnitude of the flow field. Hence, if for a given situation at time $t = t_0$ a forecast is wanted at time $t = t_1 > t_0$, the period of time between t_0 and t_1 must be separated in a finite number of time intervals Δt and the solution of (22) at $t = t_1$ is achieved by *time stepping*, calculating the temperature distribution at $t = t_0 + \Delta t$ from the distribution at $t = t_0$, that at $t = t_0 + 2\Delta t$ from the previous time level $t = t_0 + \Delta t$, etc. until t_1 is reached.

The procedure as described above is applied to the entire set of equations, thus, for every time step, $I \times J \times K$ solutions of (7)–(12) and (5) have to be calculated, a task which can only be performed by computers. In addition, it should be noted that the numerical schemes used in (22) and (23) are elementary and were only selected in order to demonstrate how numerical procedures work. In practise, far more sophisticated higher order finite difference schemes are used and applied to *staggered grids*, i. e. instead of just one grid for all variables, different grids depending on the type of the variable are used simultaneously.

2.4 How a forecast model works

Nowadays, there are many types of forecast models in use all over the world applied to a wide spectrum of spatial and temporal scales. Acccording to their task, they are different with respect to the physical processes included, the formulation of the finite difference equations may vary, and they use different grids. For example, the forecast time scale of a model designed for predicting the evolution of large scale circulation patterns in response to climate change on earth is of the order of decades. As climate changes occur on global scales, it is sufficient to use a low resolution spherical grid covering the whole earth. It is not necessary to include high frequency physical processes, but special care has to be taken to model the interactions between ocean and atmosphere correctly. By contrast, the forecast time scale for a regional model designed for short range prediction of currents in a shelf sea area is of the order of days. Therefore, it has to take account of processes occurring on similar timescales, e. g. tides, the actual weather conditions, etc., and high resolution is required to resolve the bathymetry and coastlines properly. In addition, special care has to be taken to parameterize adequately the effects of sub-gridscale processes. Although the design of forecast models is task specific, the procedure in order to carry out the task is essentially the same. This is sketched in Figure 2 and will be discussed in the following.

The very first step to set up a forecast model is *creating the model code* in a way that solutions of the govering equations can be calculated by computers. This involves the discretization of the differential equations, i. e. the finite difference formulation as shown above, and the encoding in any computer language. This is a rather complicated and expensive task, which is already done in ready to use models. However, the next step, the *setup of the model domain and the grid*, has to be done on one's own by every user according to the posed problem.

The choice of the geographical boundaries of the model domain depends on the geographical area of interest; they are defined in terms of four parameters, $\lambda_0, \lambda_1, \varphi_0$, and φ_1, denoting longitude and latitude circles bounding the domain in the west, east, south and north, respectively. Because of the curvature of the earth, the so–defined area is not a rectangle, which causes trouble when defining a Cartesian grid. If the area is small enough that curvature effects may be neglected, a common method to overcome this problem is to map the area on a horizontal plane, for instance by Mercator projection. Otherwise, spherical coordinates have to be used. The horizontal grid is defined by separating the model domain in $I \times J$ (see above) grid cells. The size of the grid cells depends on the wanted horizontal resolution and on the available computer power, making oneself clear that the required computer resources are proportional to the number of grid cells. In order to cover the full vertical range of the ocean, the definition of the vertical grid requires some previous knowledge on the bottom topography in the model domain. The vertical grid may

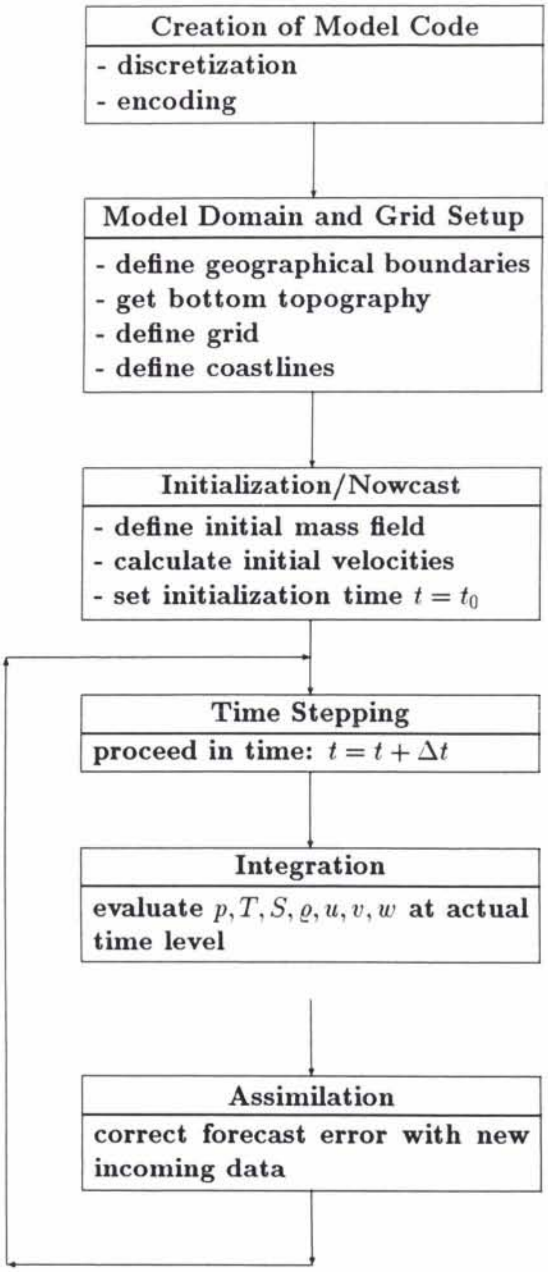

Figure 2 *Working procedure of a forecast model.*

Report no. changed (Mar 2006): SR-292-UU

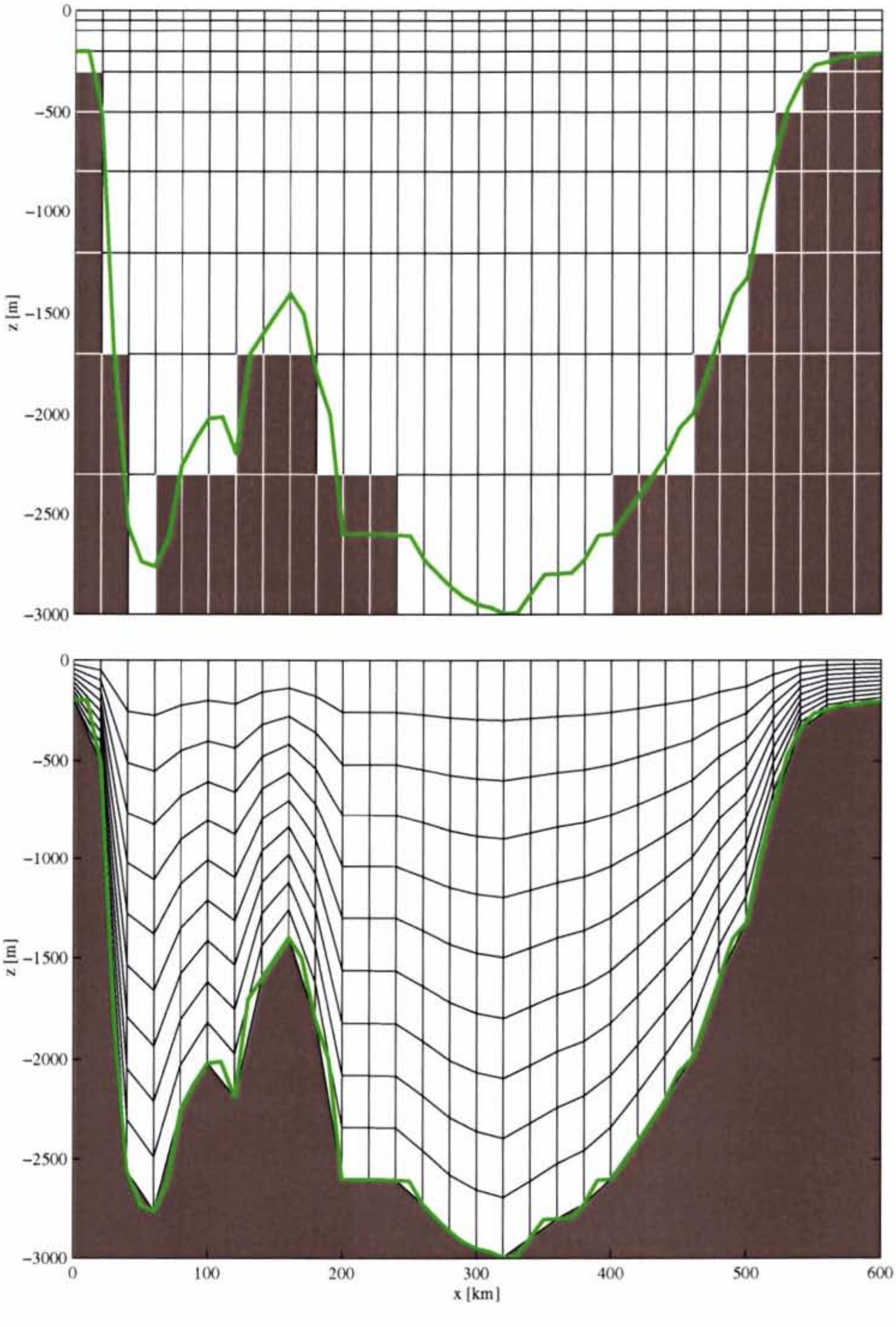

Figure 3 *Arrangement of grid cells in z- (top) and sigma coordinates (bottom) in the x–z plane of an arbitrarily chosen model domain with 20 km horizontal resolution. The number of layers is the same in both cases. White cells contain water, dark cells land. The original bottom topography (10 km resolution) is indicated by the green line.*

then be arranged in a way that the water column is divided in K layers of vertical extent Δz, where Δz is allowed to vary with depth but does not vary horizontally (Figure 3). In this case, the vertical coordinates of the model are horizontal and are called *z-coordinates.* The major disadvantage of these coordinates is that steep topography is not well resolved and shallow water regions are represented by only a few layers. Alternatatively, *sigma coordinates* may be used dividing the water column at every horizontal position in K layers between the sea surface and the bottom, hence the same number of vertical levels is provided everywhere and the shallow areas are resolved by the same amount of vertical levels. As the vertical extent of the layers varies from place to place according to the water depth, such coordinates are also called *terrain following coordinates.* In a z-coordinate model, the implementation of bottom topography is simply performed by defining dynamically inactive "dead" grid cells (the dark ones in Figure 3). Analogously, coastlines are generated by defining "dead" and "alive" grid cells in the horizontal plane, representing land and water points, respectively.

At time level $n+1$, the prognostic variables can only be computed, if they are known at the previous time level n (cf. (23)). Therefore, an *initialization* is required for all variables at time level $n = 0$. This is done by defining the three-dimensional initial mass field in terms of an initial distribution of T and S and then calculating ϱ. The initial T and S values may either be obtained from actual measurements or from climatological data bases. They may also be constructed artificially, if it is intended to study a special situation. If direct measurements of the velocity field are available, these may be used as initial velocities, but, because measurements contain errors and high-frequency and large wavenumber contributions which are not resolved by the model, the velocities must be adjusted in a way that they satisfy dynamical constraints imposed by the model physics. In practise, one makes use of the fact that seawater is nearly incompressible, hence assuming $d\varrho/dt = 0$. The continuity equation ((2), (10)) then simplifies to

$$\frac{\partial u}{\partial x} + \frac{\partial v}{\partial y} + \frac{\partial w}{\partial z} = 0, \tag{24}$$

which means that the divergence, that is the net flux through the six sidewalls of every grid cell, must be zero. In order to achieve that, the divergent part of the velocity field is calculated by iterative methods and then removed from the measured velocities. If no direct measurements are available, one has no choice but computing the geostrophic velocities from the pressure field. In any case, if T and S originate from actual measurements, the initialization fields also represent a nowcast for the time $t = t_0$.

The next three steps, *time stepping*, *integration* and *assimilation* occur in a loop, which is executed as many times as the user wants. After initialization, the model advances forward in time by one time step Δt to model time $t = t_0 + \Delta t$. Integration means solving the model equations (7)–(12) and (5) for the prognostic variables at

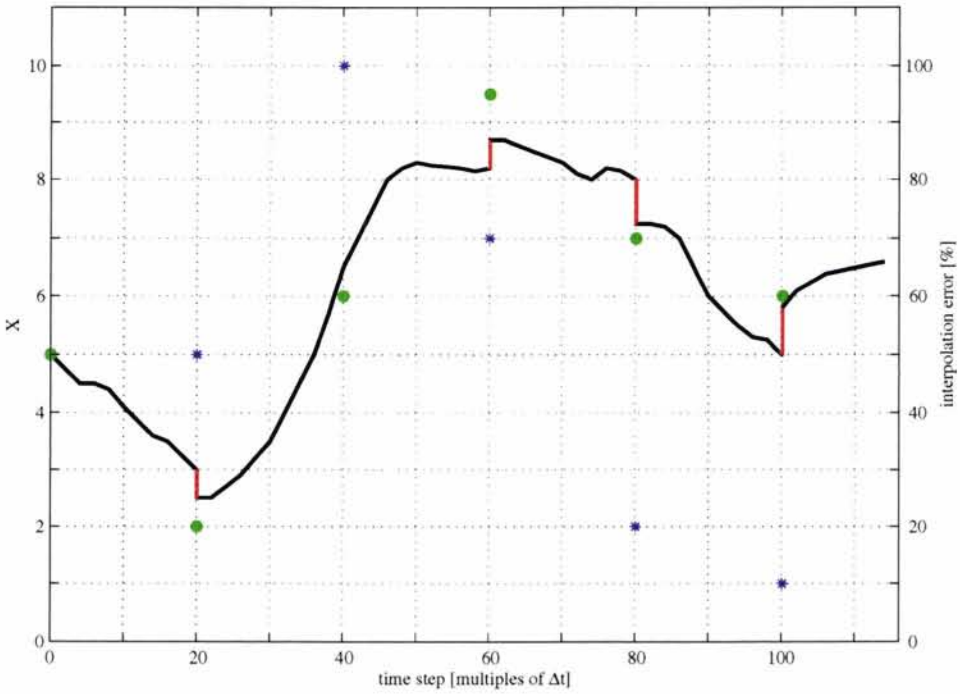

Figure 4 *Intermittent updating of a forecast model by data assimilation (sketch). The numerical solution (black line) of an arbitrary prognostic quantity* X *at an arbitrary position is corrected by observations (green dots) at time steps* $20 \cdot \Delta t, 40 \cdot \Delta t, \cdots, 100 \cdot \Delta t$. *The correction is indicated by red lines. Blue asterisks denote the interpolation error. Note the strong weighting of observations where the interpolation error is small.*

model time, and assimilation is a procedure for updating the actual solution of the model with data from measurements sampled in real time at $t > t_0$. Such a "correction towards reality" is desirable, because the model solution may be incorrect due to many reasons, some of which will be addresses below:

- Bad fields for initialization. This may be caused by using wrong climatologies, too coarse measurements, inadequate averaging procedures, or by assuming a wrong level of no motion for the calculation of the geostrophic initial currents.
- Unresolved physical processes, i. e. processes occurring on scales smaller than the grid scale are underrepresented or not well parameterized.
- Atmospheric forcing (wind, heating, cooling) is not well enough known.
- Insufficient formulation of boundary conditions.
- The truncation error of the finite difference equations may add up during the course of the integration.

The algorithms for assimilating data into models were originally developed for weather forecast models and have then been adopted for ocean forecasting. At runtime, the numerical solution of such models is corrected with incoming observations from weather stations. Problems arise due the fact that the observations are unevenly distributed in space and time, because the positions of the stations do not coincide with the grid points of the model, and at a given time observations are only available from a subset of stations. In addition, the horizontal resolution of the station network is normally lower than the resolution of the model. Therefore, at discrete time levels, the observations are first interpolated in space and time on the model grid. Simultaneously, a map of the interpolation error provides information on the reliability of the interpolated observations at every grid point, depending on the number and distance (in space and time) of observations contributing to the value of the physical variable at this point. The updating of the numerical solution is then performed at every grid point by melding the predicted value with the interpolated one, giving high weight to the interpolated observations where the interpolation error is small, and more weight to the numerical solution where the interpolation error is higher (Figure 4). By this method, the numerical solution is forced to satisfy the observations where observations are available, and is less affected in regions of coarse sampling.

3

The hydrographic data set

The hydrographic data set comprises 107 CTD (Conductivity-Temperature-Depth) casts collected by *NRV Alliance* and *TCG Çubuklu* in the Antalya Basin (Eastern Mediterranean) during leg 1 of the POYRAZ97 survey from 8 to 13 February 1997. All casts extend from the sea surface to a maximum depth of about 1000 m, the vertical resolution is 1 m. A complete description and analysis of the data set is provided by [7] and [8]. Therefore, only the necessary details will be given here.

Leg 1 was divided in two surveys (referred to as leg 1/1 and 1/2) 8–11 February and 11–13 February, respectively, and covering the same geographical area twice within about a week (Figure 5). CTD casts were taken on a regular grid with meridional spacing of $10'$(18.52 km) and zonal spacing $20'$($\approx$ 30 km). CTD casts on leg 1/2 were taken nominally at the same positions as on the previous leg.

For the nowcasting and forecasting experiments the data set is divided in four subsets (Figure 6). As the leg 1 survey was conducted by two vessels, there is an overlap of about 18 hours between legs 1/1 and 1/2. Therefore, subset A comprises all CTD casts taken before 11 February 16:00h (UTC) and subset B all casts taken after that time. Subset A will be used for initialization of HOPS and B for validating the model forecast. For validation of the nowcast, subset A (excluding the line of casts along 30°40′E) is further subdivided in A1 and A2, where A1 is a subset of A at half the horizontal resolution and A1 is the complement.

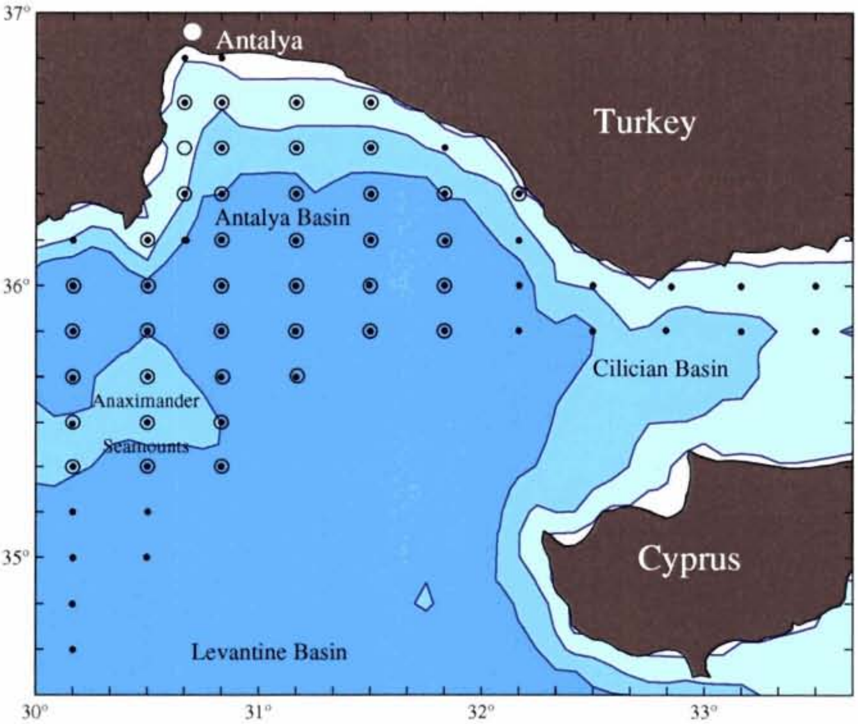

Figure 5 *Positions of CTD casts on leg 1/1 (dots) and leg 1/2 (open circles) of the POYRAZ97 survey. Water depths are indicated by 200 m, 1000 m and 2000 m depth contours.*

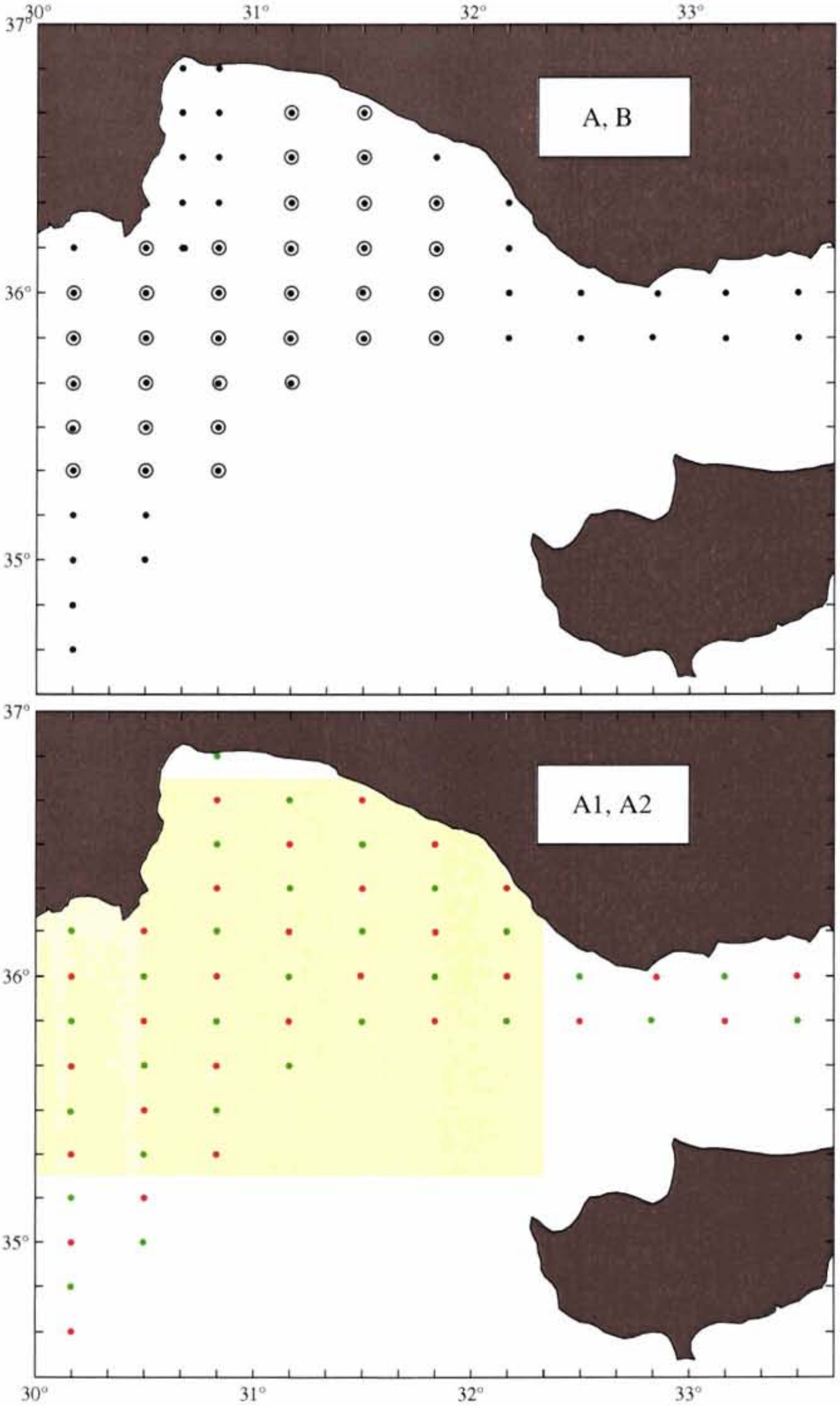

Figure 6 *Top: Data subsets A (dots) and B (open circles). CTD casts of A were taken before 11 February 16:00h, those of B later. Bottom: Data subsets A1 (green dots) and A2 (red) are subsets of A. A1 was selected at half the nominal horizontal resolution of A and A2 is the complement. The yellow area indicates the casts used for comparison with climatology (see Section 5).*

4

HOPS model domain and grid setup

The HOPS model domain comprises a rectangular area centred at 31°30′E, 35°30′N, which encompasses the area of the POYRAZ97 survey. In west–east direction it is divided in 116 and in south–north direction in 86 grid intervals $\Delta x = \Delta y =$ 4 km, respectively (Figure 7 (top)). Hence, the western and eastern boundaries are approximately $\lambda_0 = 28°56'$E, $\lambda_1 = 34°04'$E, and the southern and northern boundaries $\varphi_0 = 33°57'$N, $\varphi_1 = 37°03'$N, respectively. The horizontal grid size of 4 km was selected in order to resolve small eddies and the front of the Asia Minor Current (cf. [7] and [8]).

In the vertical, the water column is divided in 77 layers. *Double sigma coordinates* ([9]) are used, which are similar to sigma coordinates (cf. Figure 3), but with higher resolution in the upper ocean and near the bottom (Figure 7 (bottom)). The high vertical resolution of nominally 10 m in the upper about 450 m was found necessary for resolving adequately minima and maxima of the sound velocity distribution.

Bottom topography data at $5' \times 5'$ horizontal resolution were obtained from [10]. In order to minimize the truncation error of the finite difference equations over steep topography, the arrangement of vertical levels must satisfy the *hydrostatic consistency condition* ([11]). In the present case, this was achieved by iterative smoothing of the topography by a median filter until no changes occurred and subsequent application of a local smoother in areas where the hydrostatic consistency condition was not yet satisfied (for details see [9]). The final product together with the raw topography is shown in Figure 8.

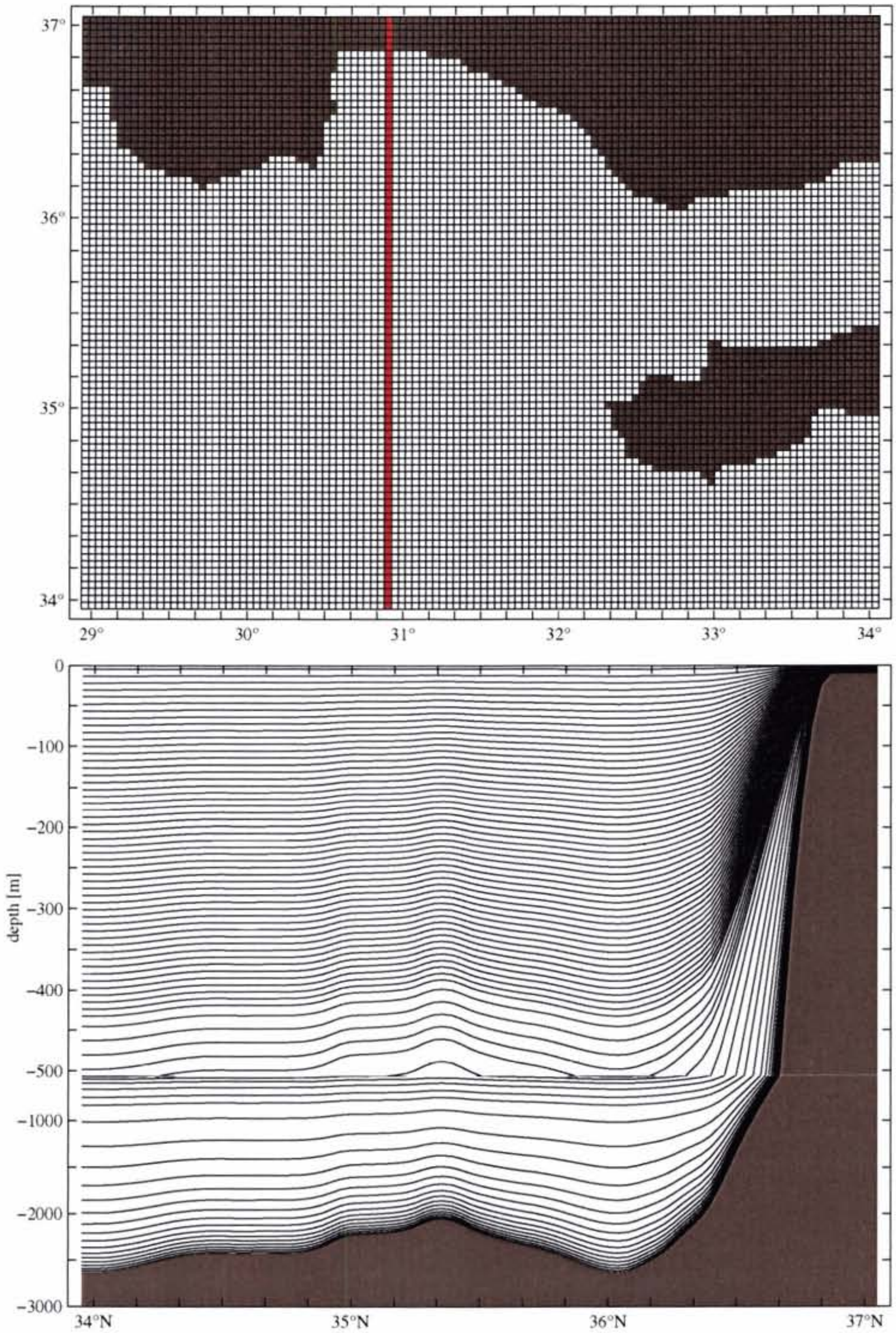

Figure 7 *Horizontal (top) and vertical grid (bottom) of the HOPS model domain. The red line denotes the position of the vertical section shown in the bottom panel. Note the change of depth scale below -500 m.*

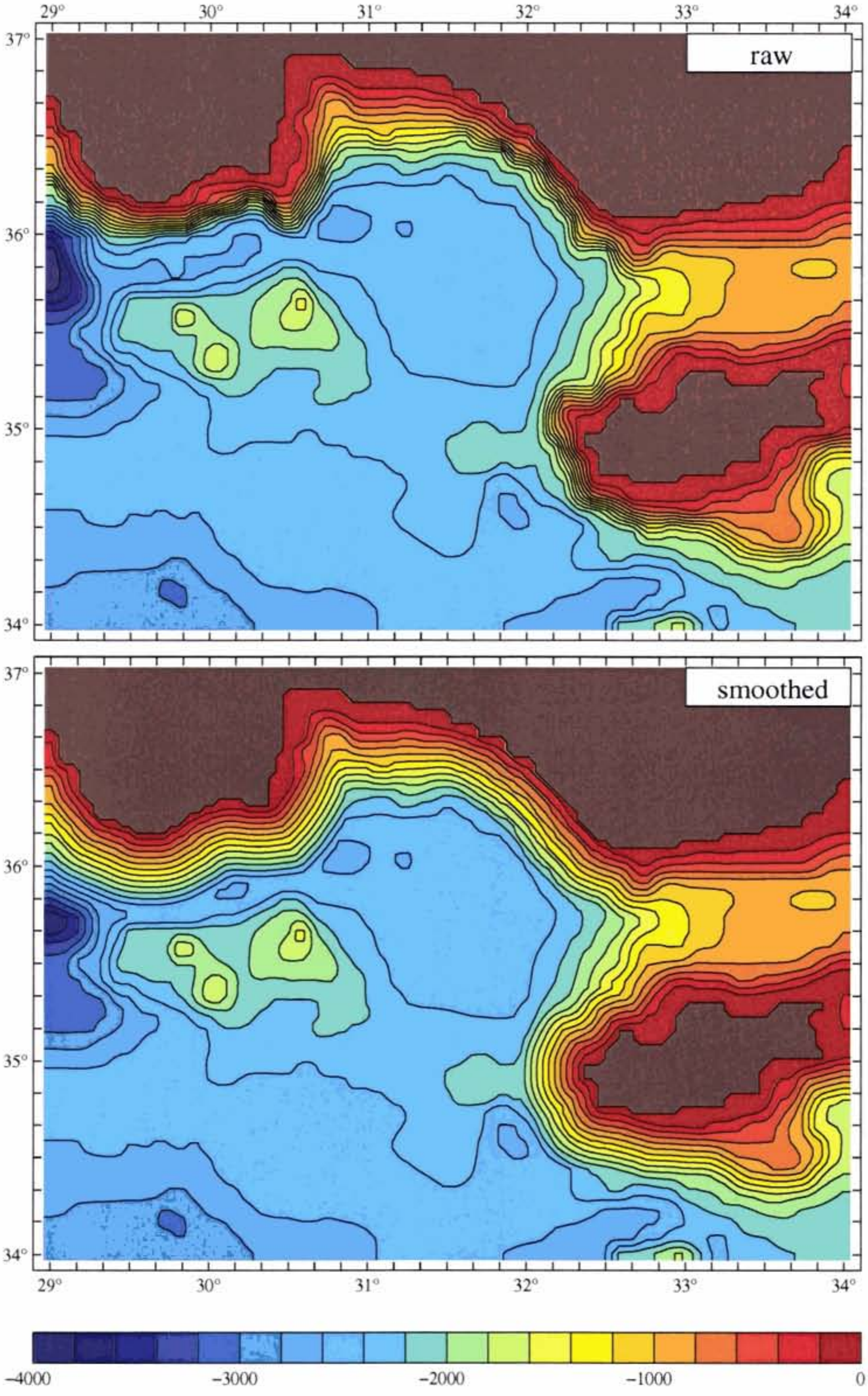

Figure 8 *Raw and smoothed bottom topography. Smoothing is necessary in order to minimize the truncation error over steep topography. Note the reduced shelf slope after smoothing. Water depths are in metres.*

5

Shortcomings of climatologies

Before, in the next section, we demonstrate and compare methods for nowcasting the sound velocity field from a limited set of observations, the importance of at least sparse measurements is pointed out by comparison with two commonly used standard climatologies, named GDEM (General Digital Environmental Model) and MODB (Mediterranean Ocean Data Base).

GDEM is a worldwide monthly climatology with variable horizontal resolution. It was created using all temperature and salinity profiles available from MOODS (Master Oceanographic Data Set), which is the oceanographic data base of the United States Navy. MOODS contains about seven million observations and is based on over 70 years of data. For the Mediterranean, GDEM is available a horizontal resolution of 10′. For the present study, it was obtained from NAVOCEANO (Naval Oceanographic Office, Stennis Space Center, Mississippi) via the Internet address "http://www.navo.navy.mil/". For a technical discussion of how GDEM was derived from MOODS, the reader is referred to [12].

MODB is a seasonal climatology of the Mediterranean Sea at 15′ resolution provided by the University of Liège (Belgium). It is available on the Internet at "http://www.modb.oce.ulg.be/". From MODB, there exist three successive releases MED2, MED4, and MED5, from which the first is used for this study. MED2 is based on the BNDO (Bureau National des donnees oceanographiques) file containing bottle profiles collected in the Mediterranean since the begin of the century, and on worldwide CTD and bottle data of the NODC (National Oceanographic Data Center). A full description of the data set, the analysis technique and the results is provided by [13].

For comparison, the measured sound velocity profiles from data subsets A1 and A2 (cf. Fig. 6) are plotted together with those obtained from the GDEM February and MODB-MED2 winter climatologies in Figs. 9 and 10 at their respective locations. As the positions of the measured profiles match exacly those of GDEM, it was possible to assign an individual GDEM profile to every measured one, except for subplots 83 and 93, where no GDEM profile was available. For MODB-MED2, due to the lower resolution, each measured profile was combined with its next neighbour from climatology as long as the difference in position did not exceed 5′ in latitude or longitude, which was the case for subplots 61, 62, 83, 93, and 95.

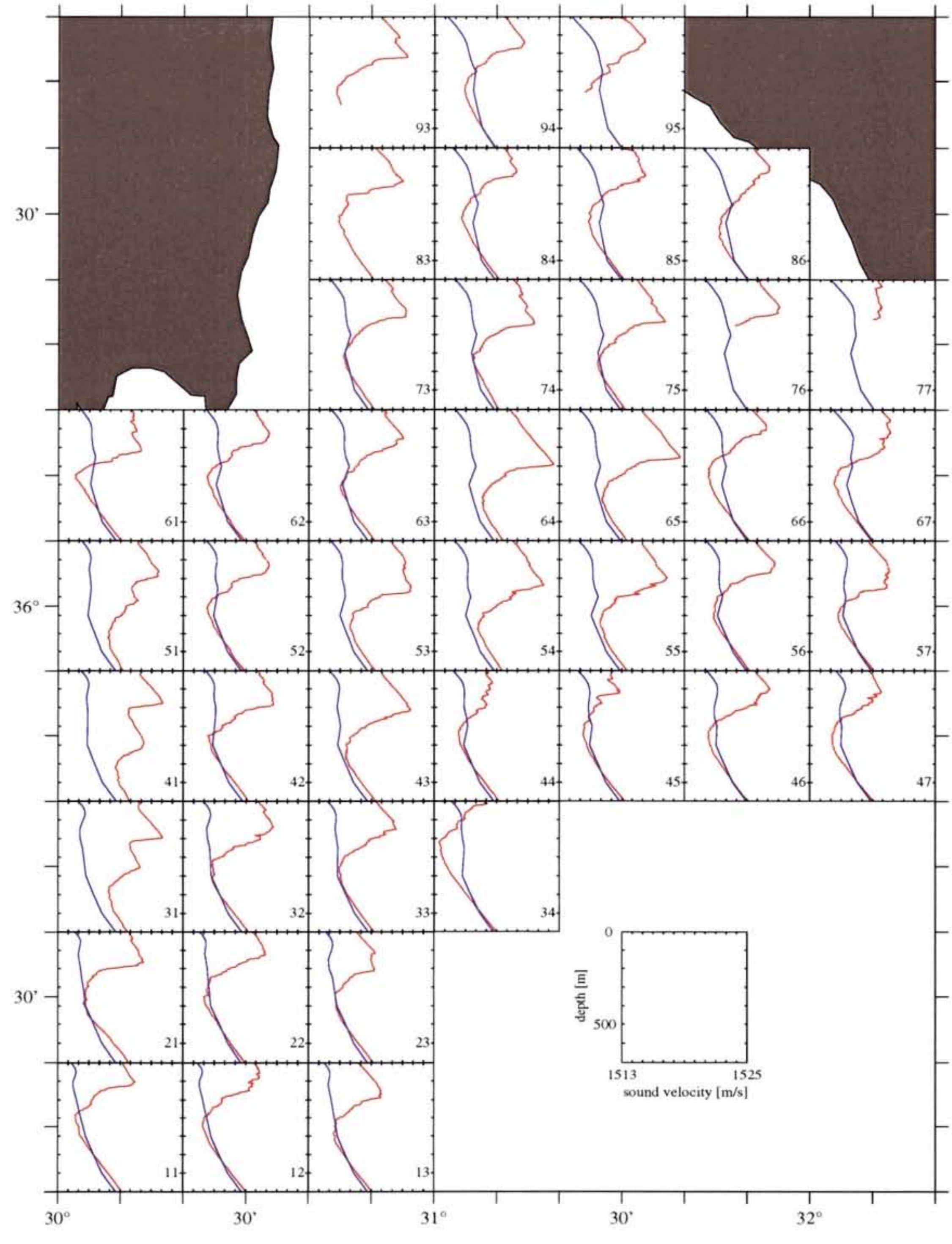

Figure 9 *Sound velocity profiles from measurements and climatology. Red: measured profiles of data subsets A1, A2. Blue: profiles from GDEM February climatology. The centre of each subplot corresponds to the positions of the profiles, numbers in the lower right corner of the subplots serve for identification.*

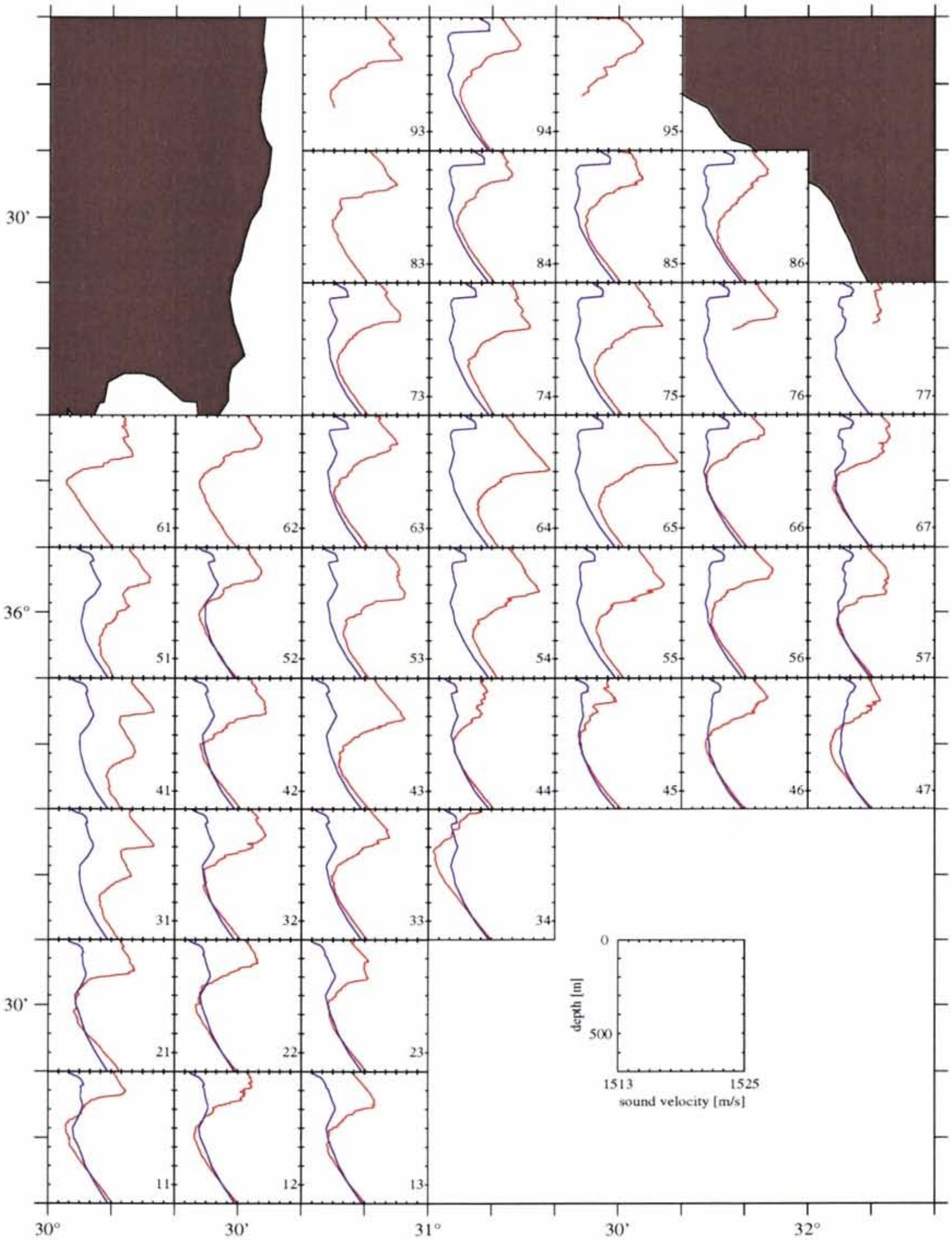

Figure 10 *Sound velocity profiles from measurements and climatology. Red: measured profiles of data subsets A1, A2. Blue: profiles from MODB-MED2 winter climatology nearest to the measured ones. The centre of each subplot corresponds to the positions of the measured profiles, numbers in the lower right corner of the subplots serve for identification.*

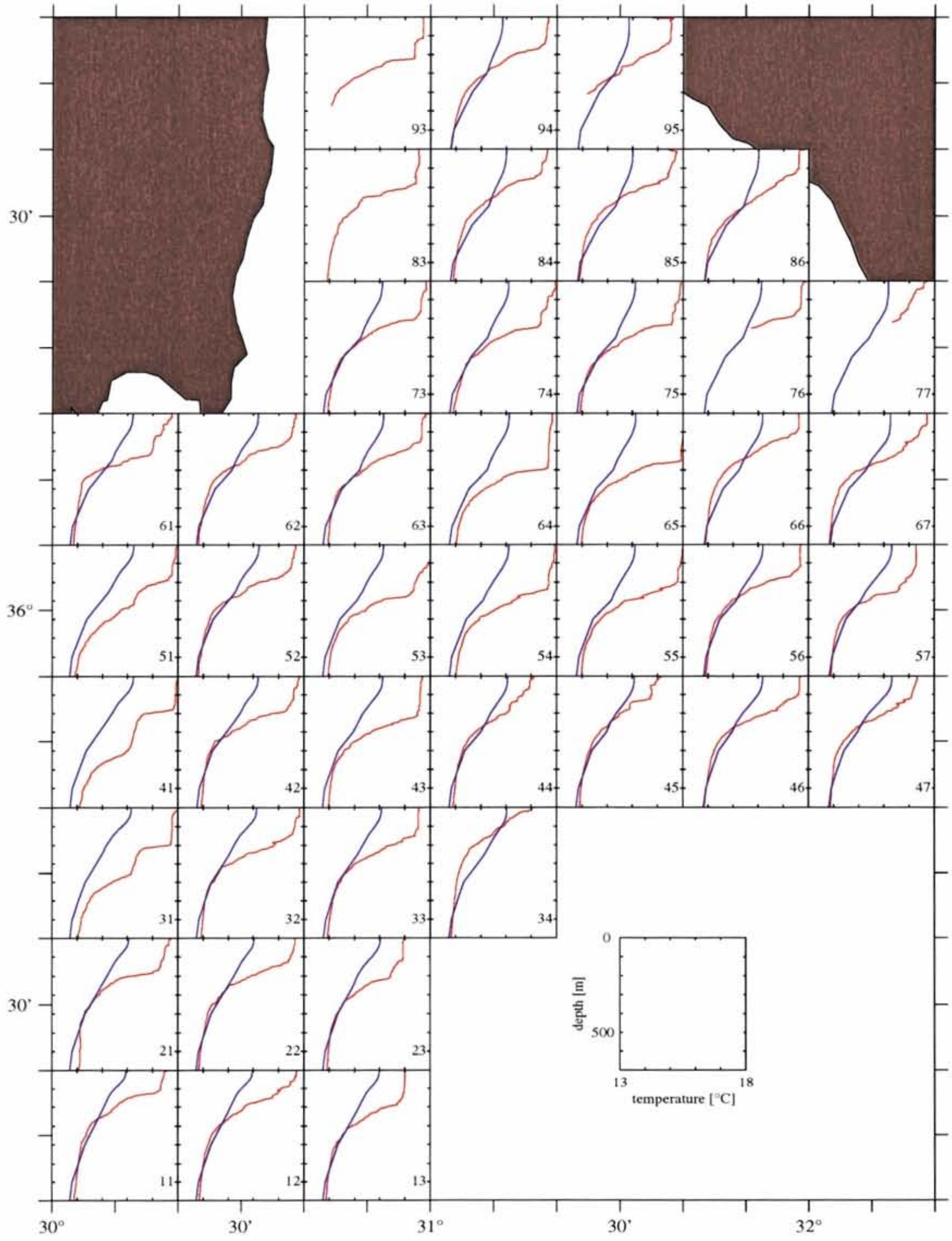

Figure 11 *Same as Fig. 9 but for temperature.*

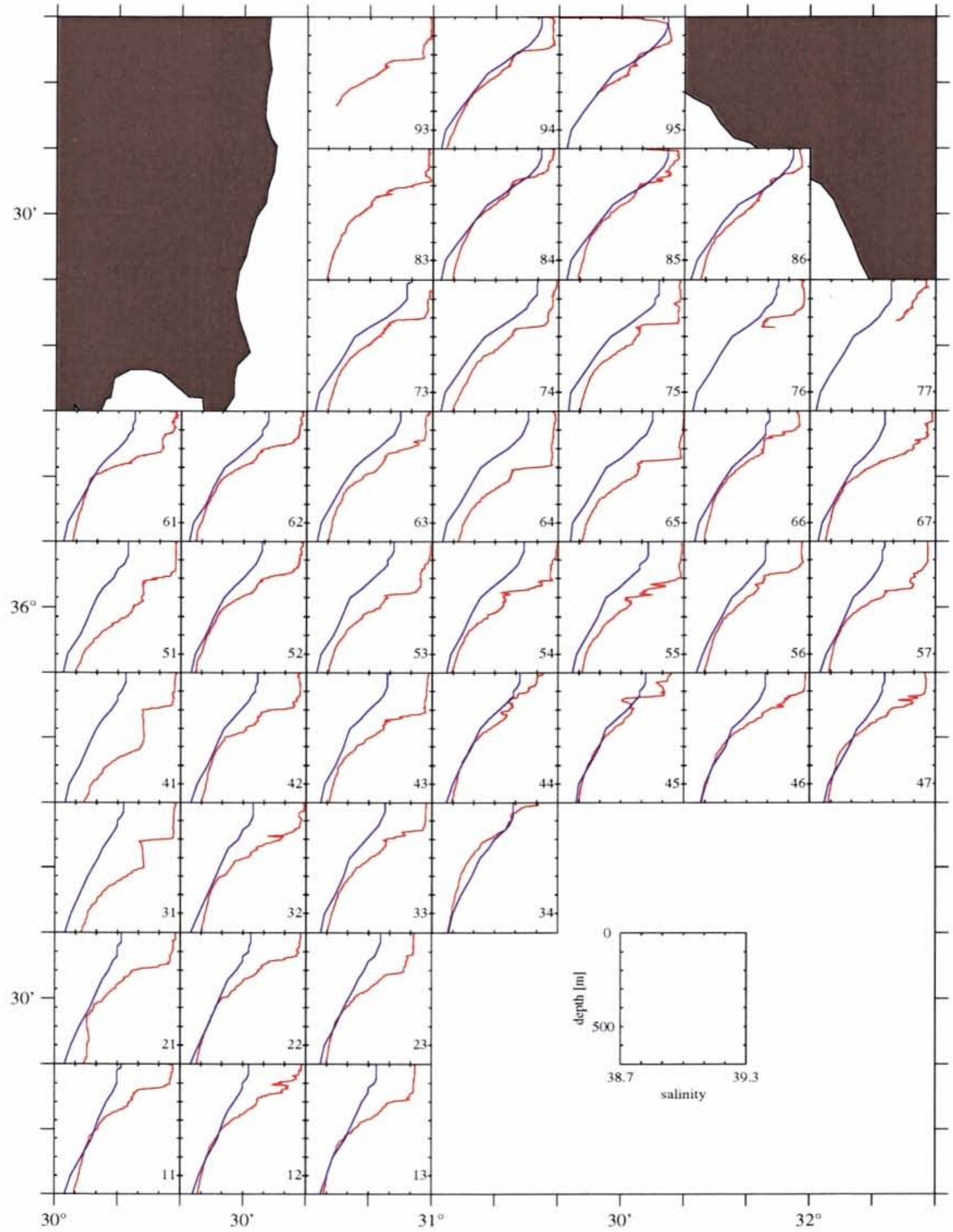

Figure 12 *Same as Fig. 9 but for salinity.*

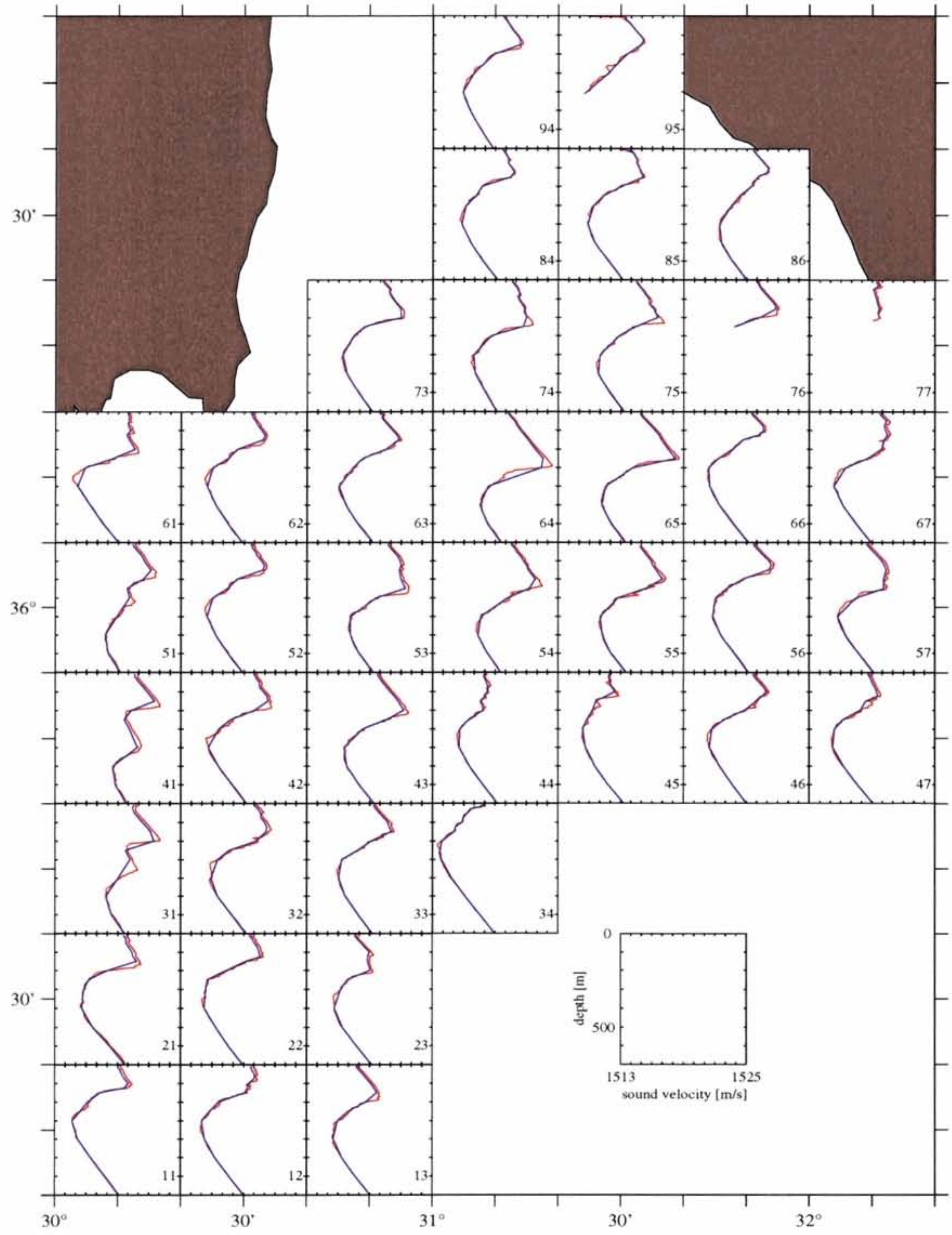

Figure 13 *Sound velocity profiles from measured temperature combined with climatology salinity. Red: measured profiles of data subsets A1, A2. Blue: profiles calculated from CTD temperature and GDEM February salinity. The centre of each subplot corresponds to the positions of the measured profiles, numbers in the lower right corner of the subplots serve for identification.*

A discussion on the difference between the profiles can be held short — the sound velocity profiles from both climatologies do not match at all those from actual measurements. The deep and near surface sound channels, which are well pronounced in almost every measured profile, are not reproduced by GDEM in any case, and MODB-MED2 reveals only in a few cases something which might be called a sound channel, but at a wrong depth. In addition, the climatological sound velocity deviates by up to 10 m s^{-1} from the measured one in the upper about 400 m depth range. Fig. 11 reveals the cause for the deviations; the GDEM temperature over that depth range is far too low, in many cases the difference exceeds 2 K. For completeness, the corresponding picture is also shown for salinity (Fig. 12). In the same way as with temperature, the climatology salinity is too low. Similar pictures were also obtained from MODB-MED2, but they are not shown here, because they do not add anything new.

One might argue that the large differences between measurements and climatology are due to the fact that the hydrographic conditions in the Antalya Basin in February 1997 were anomalous. This may be true, but this is also the point: The ocean exhibits high variability in space and time, also interannually. Thus, the stratification of temperature and salinity of February 1997 is *expected* to be different from the situation in the same month of another year. As a climatology is representing a long-term mean based on averaging many measurements, the natural horizontal, vertical, and temporal variability is removed. Therefore, it is unlikely that a climatology matches a real situation obtained from direct measurements.

As sound velocity depends on temperature, salinity, and pressure, it should, whenever possible, be determined from simultaneous measurements of the three basic quantities by CTD or XCTD. If, for any reasons, this is not possible, it is a good compromise to measure only temperature by XBT, and to recalculate the sound velocity from XBT temperature and climatological salinity profiles. This is illustrated by Fig. 13, where the sound velocity was calculated from the CTD temperature profile, the GDEM salinity profile at the corresponding position, and pressure. Small disagreements between the blue and read curves are mainly caused by vertical resolution, which is lower in GDEM than from the measurements.

6

Nowcasting of sound velocity structure

In the present situation, nowcasting means to provide the best estimate of the three-dimensional distribution of sound velocity on 11 February 16:00h using data set A. To explore the nowcasting capabilities of HOPS, the reduced data set A1 is used for calculating the sound velocity structure at the A2 positions applying two different methods. The first method (denoted Method I) is not based on HOPS. It is a linear horizontal interpolation scheme with inverse distance weighting. The HOPS method (Method II) is an optimized linear interpolation, which makes use of the knowledge of the horizontal scales governing the dynamics of this region. The products of both methods are compared to each other and validated against the measured profiles at the A2 positions.

As the CTD casts of subsets A1 and A2 (Figure 6) are nominally arranged on a equally-spaced latitude/longitude grid, it is convenient for Method I to assign a pair of indices (j, i) in matrix notation to each cast (Figure 14), where j is the row index and i the column index. Sound velocity profiles at 10 m vertical resolution are then evaluated from temperature, salinity, and pressure of all A1 (green) casts, and the sound velocity at the A2 (red) positions is calculated at every level according to the horizontal interpolation scheme

$$V_{j,i} = a_1 \cdot V_{j,i-1} + a_2 \cdot V_{j,i+1} + a_3 \cdot V_{j-1,i} + a_4 \cdot V_{j+1,i}, \tag{25}$$

where $V_{j,i}$ is the interpolated sound velocity at the A2 position denoted by the pair of indices (j, i), and $V_{j,i-1}, V_{j,i+1}, V_{j-1,i}, V_{j+1,i}$ are the A1 sound velocities at the neighbouring western, eastern, southern and northern cast, respectively. The weighting coefficients

$$a_l = \left(d_l \sum_{k=1}^{4} \frac{1}{d_k} \right)^{-1} \tag{26}$$

are inverse proportional to the distances d_l between the A2 and the neighbouring four A1 casts.

Method II is based on standard objective analysis techniques (see [14]). In contrast to Method I it takes account of all observations instead of only the neighbouring ones, and assumptions have to be made for the correlation between the sound velocity at the interpolated position and the observed sound velocity, and for the correlation of the observations among themselves (see below). The sound velocity V_r at any

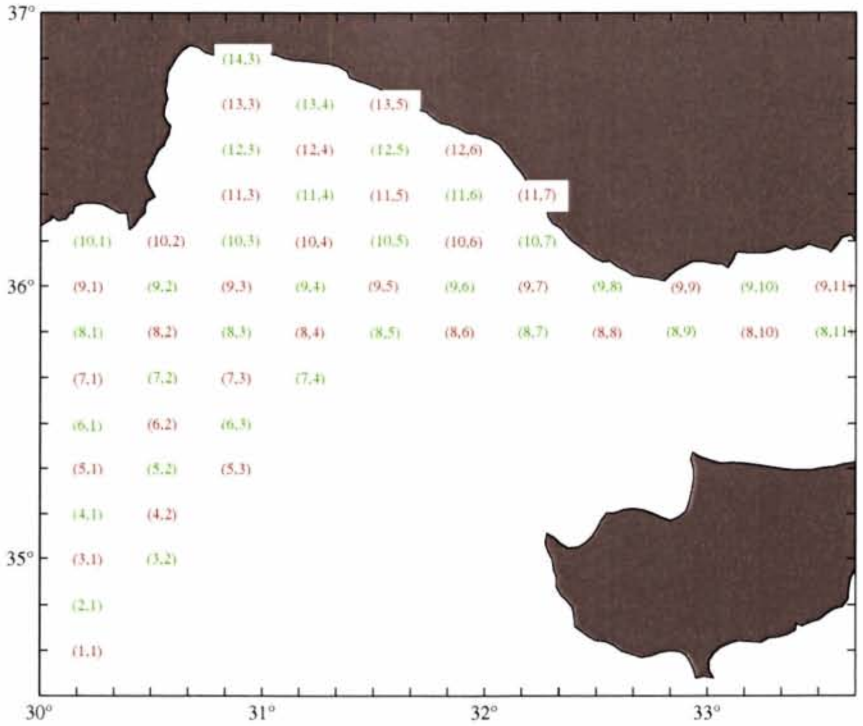

Figure 14 *Index scheme applied to the A1 (green) and A2 (red) CTD casts (cf. Figure 6).*

horizontal position (x_r, y_r) is optimally linearly interpolated (in a least squares sense) by the formula

$$V_r = \sum_{m=1}^{N} \beta_{rm} \left(\sum_{s=1}^{N} \alpha_{ms}^{-1} V_s \right), \tag{27}$$

where N is the number of CTD casts of A1, and V_s is the observed sound velocity of the s-th cast at position (x_s, y_s).

$$\beta_{rm} = C(V_r, V_m) \tag{28}$$

is the correlation matrix between the sound velocity at the interpolated position and the m-th cast and

$$\alpha_{ms} = C(V_m, V_s) + E\delta_{ms}. \tag{29}$$

Here, $C(V_m, V_s)$ is the correlation between the m-th and s-th cast, E the error variance of all casts and δ_{ms} the identity matrix.

For sufficiently large data sets, the correlation function C may be calculated from the data. In the present study, however, a simple analytical function

$$C = \left[1 - \left(\frac{d}{\Lambda}\right)^2\right] exp \left[-0.5 \left(\frac{d}{\Gamma}\right)^2\right] \tag{30}$$

is used instead, where d is horizontal distance. The crucial point is the definition of the e-folding (or correlation) scale Γ and the zero-crossing scale Λ, because these parameters determine the relative weight of every measured sound velocity profile. A natural e-folding scale is the *internal Rossby radius of deformation* (or simply, the *Rossby radius*) R_D. Its physical meaning is that for motions at this horizontal scale the buoyancy force (hidden in the gravitational force $\mathbf{F}_g$ of equation (1)) and the Coriolis force are of the same order of magnitude. For larger scale motions, the Coriolis force is dominant and at scales smaller than R_D prevails the buoyancy force. In practice, R_D is approximately equal to the radius of mesoscale eddies, which is a meaningful correlation scale. If no information on eddy sizes is available, R_D can be estimated from CTD casts as

$$R_D = \frac{1}{f}\sqrt{gH\frac{\varrho_2 - \varrho_1}{\varrho_2}}, \tag{31}$$

which requires to approximate the measured density profile by a representation of two homogeneous layers with densities ϱ_1, ϱ_2 in the upper and lower layer, respectively. In the present situation, a mean density profile was calculated from all A1 CTD casts. The thickness of the upper layer was estimated as $H = 150$ m, and the densities as $\varrho_1 = 1029$ kg m^{-3} and $\varrho_2 = 1031$ kg m^{-3}, which yields $R_D \approx 20$ km.

An inherent shortcoming of Method II is that it produces unreasonable values at locations, which are too far away (that is more than the zero-crossing scale) from observations. Therefore, it is a convenient method to define a background field which is previously subtracted from the observational values, and the objective analysis is performed only on the anomalies. Subsequently, the background field is added to the anomaly field. By this method, the final product approaches the value of the background field at locations which are far away from observations, because the objectively analyzed anomalies tend to become very small there due to the reduced correlation expressed by (28). Usually, climatologies are serving well as a background field, in the present case, however, the available winter climatologies GDEM and MODB-MED2 (see Section 5) for this region were found to be considerably colder and less saline then the POYRAZ97 survey. Therefore, the horizontal mean value of all observations was used as background field at each horizontal level.

In the same way as for Method I, sound velocity of all A1 CTD casts was calculated at 10 m vertical resolution and then evaluated at the A2 positions applying equation (27). As $R_D = 20$ km is only a first guess for the correlation scale Γ, the calculations were repeated for different scales between $\Gamma = 15$ km and $\Gamma = 25$ km each in combination with a zero-crossing scale between $\Lambda = 1.5\Gamma$ and $\Lambda = 2.5\Gamma$. The best result, i. e. sound velocity profiles with minimum deviation from the A2 validation profiles at the respective position, was obtained for $\Gamma = 22$ km and $\Lambda = 44$ km. As the HOPS objective analysis scheme also allows a time-difference weighting of the observational data, 10 February 1997 00:00h is selected as the instant for the analysis and a temporal correlation scale of $\tau = 100$ days was applied; thus all A1

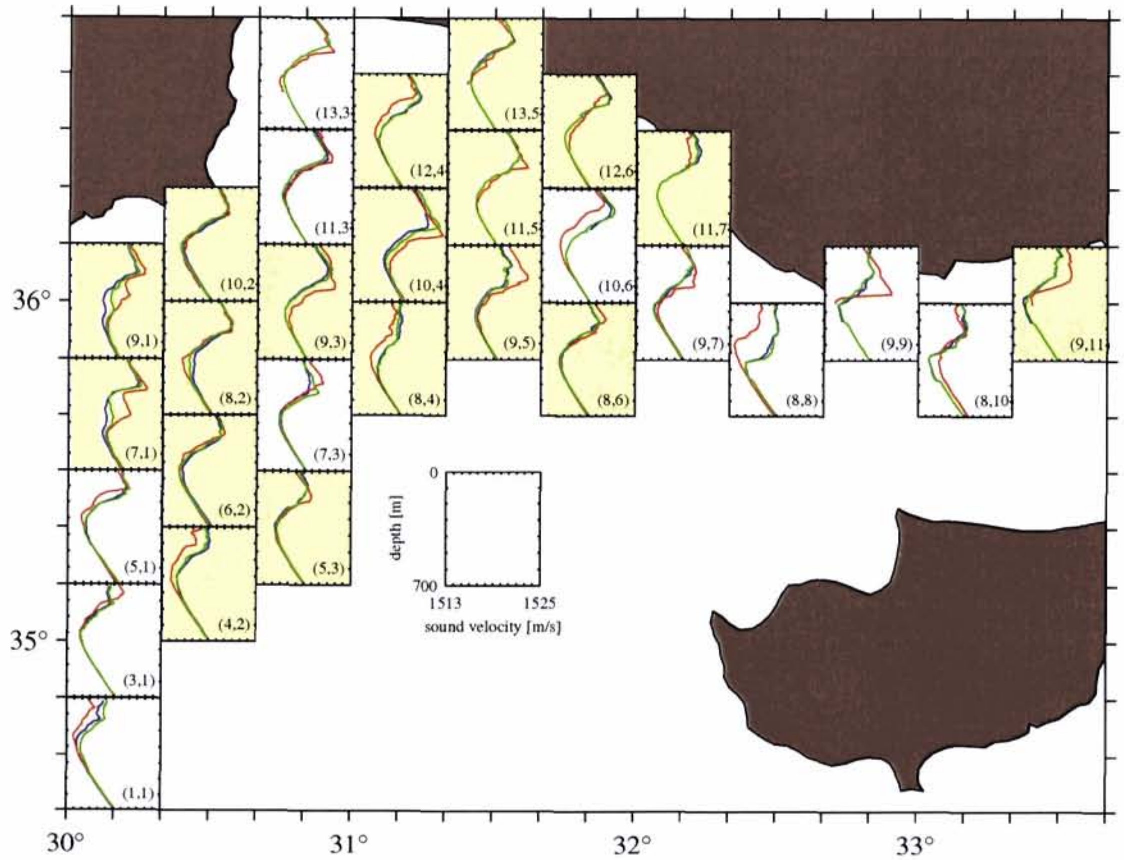

Figure 15 *Nowcast of sound velocity profiles at positions of A2 casts from interpolation of A1 casts (cf. Figures 6 and 14) using Method I (blue profiles) and Method II (green). The A2 validation profiles are red. All profiles correspond to the centre position of each subplot, numbers in parentheses correspond to the indices in Figure 14. For the meaning of the coloured axes back panels see text.*

data are approximately weighted equally in time.

The nowcasted profiles, together with the corresponding ones from Method I and the validation profiles, are displayed in Figure 15 at 29 positions corresponding to the red indices in Figure 14. For assessment of their quality, the mean difference

$$\Theta_{I,II} = \frac{1}{K}\sum_{k=1}^{K} |V_{I,II}(z_k) - V_0(z_k)| \tag{32}$$

between the nowcasted profiles V_I or V_{II} and the validation profile V_0 was calculated for both methods. Here, K is the number of common depth levels of all three profiles (note that water depth may limit the length of profiles), and z_k is depth. At those locations where Θ_{II} was less than Θ_I the axes back panels of the respective subplot in Figure 15 is yellow. Hence, at 18 out of 29 locations Method II yields better results than Method I. Even after averaging Θ_I, Θ_{II} over all 29 locations including the bad ones, Θ_{II} is still slightly smaller than Θ_I. At most locations, the blue and green curves lie very close together. This is because the Method I algorithm provides already reasonable results by inverse distance weighting of the neighbour profiles, which also make the major contribution to the sound velocity estimate of Method II. At other locations, both methods yield rather bad results, for example at (7,1), (10,6), (8,8), or (9,9). This is due to the circumstance, that the distance between A1 casts (37 km meridionally, 60 km zonally) does not resolve the Rossby radius and the contribution of less well correlated profiles is increasing making the interpolated profiles less reliable. For the assessment of the reliability, Method II also provides error maps of the interpolated fields, which are based on the statistics of the input data.

Alltogether, for nowcasting the structure of sound velocity, the HOPS method is superior to simpler interpolation schemes, because it takes account of horizontal correlation scales controlled by dynamics and provides an error estimate for the interpolated values. The HOPS nowcast products will be optimal if the horizontal distance between the input profiles is equal or less than the Rossby radius. Hence, for a successful nowcast of the sound velocity structure of a particular region it is essential to take account of the Rossby radius for the design of the survey pattern.

7

Forecasting of sound velocity structure

In order to explore the forecasting capabilities of HOPS in support of ocean acoustics, the model is initialized by data set A and then integrated forward in time until the end of leg 1/2. The forecasted sound velocity profiles are validated against the measured profiles of data subset B at their respective time and position.

7.1 HOPS initialization

Initialization of HOPS requires to define initial values of temperature, salinity and the three velocity components for every cell of the three-dimensional grid, i.e. at $116 \times 86 \times 77 = 768152$ locations (cf. Section 4). This is accomplished by the following steps:

- Temperature and salinity of data subset A are mapped on the horizontal model grid by objective analysis at 101 depth levels located at 0, 10, 20, ..., 1000 m depth. In order to enable a smooth startup of the model, horizontal gradients are reduced by selecting a horizontal correlation scale of $\Gamma = 30$ km and a zero-crossing scale of $\Lambda = 60$ km, which are about 50% larger than the values previously used for the nowcast experiments. For the time-difference weighting, a temporal correlation scale τ=100 days related to 8 February 1997 00:00h is selected. This is also the model initialization time t_0. As a background field, the mean value of all observations is used at each level.
- In-situ density is calculated from the temperature, salinity, and pressure field.
- Dynamic topography, which is the vector potential for geostrophic currents, is calculated from the density distribution.
- Temperature, salinity, density, and dynamic topography are mapped on the model vertical *double sigma levels* by linear interpolation. Below 1000 m depth, the 1000 m values are used, because the CTD casts do not extend beyond that depth.
- The three-dimensional field of geostrophic currents is evaluated applying a level of no motion of 800 m according to [15] and [16].

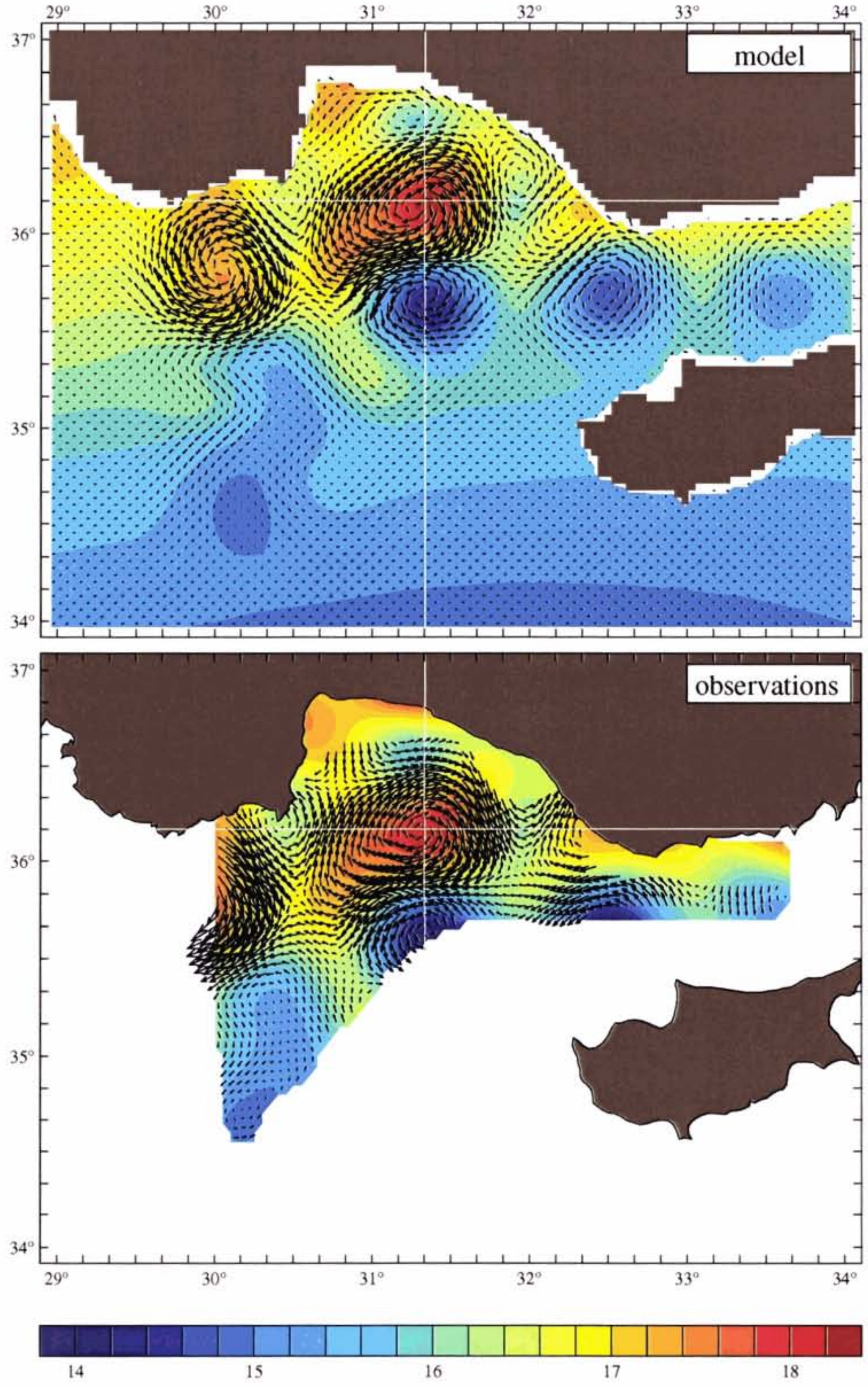

Figure 16 *Initial distributions of temperature [°C] and horizontal velocity at 200 m depth from the model and from observations. Maximum speeds are close to 40 cm* s^{-1}. *The white crosshair indicates the centre of the Antalya Anticyclone.*

As an example, the top panel of Figure 16 shows the distribution of temperature and velocity at 200 m depth. Major features are the two strong, warm anticyclones – the Antalya Anticyclone in the centre of the Antalya Basin and the Anaximander Anticyclone between the Anaximander Seamounts and the Turkish coast (cf. Figure 5), and a train of four cold cyclones south of the anticyclones and in the Cilician Basin. A comparison with the observations from leg 1/1 (bottom panel; identical with Figures 6 and 15 of [7]) reveals that the model initial distributions match nearly exactly the observed fields. Small differences are due to different grids and different methods for calculating the geostrophic velocity in the model and from observations. However, this does not imply that the dynamical situation of the model is the same as in reality, because the objective analysis output approaches the background field in regions with unsufficient data coverage. This artefact generates the isolated cold cyclones, which in reality are perhaps part of a meandering current, and the circular shape of the Anaximander Anticyclone, which is also not manifested by the measurements.

7.2 Integration and intermittent assimilation

The integration of the forecast model starts on t_0=8 February 00:00h and is carried out for seven days using a time step of 5 minutes. An output of the calculated fields is performed every 72 time steps, i. e. in six-hour time intervals. No external forcing is applied because of the lack of adequate data, that is the surface fluxes of heat, freshwater, and momentum imposed by wind forcing, are zero. On the other hand, the analysis of the meteorological data measured on *Alliance* (cf. [7]) has shown, that the wind speed was rather low during that period of time, which makes significant wind-mixing events unlikely. Somewhat more critical is the assumption of zero heat and freshwater flux, which are estimated by [7] to be of the order of -40 Wm^{-2} and 5 mm day^{-1}. These fluxes have obviously lead to surface buoyancy loss and subsequent convective overturning down to about 150 m depth. The overturning, however, is restricted to the already unstratified centre of the Antalya Anticyclone, and the corresponding changes in temperature and salinity are such small that a significant impact on the dynamical behaviour of the region can be excluded.

For a smooth startup of the model integration, horizontal gradients of temperature and salinity were reduced by applying rather large correlation scales (see above). A disadvantageous consequence of this procedure is that it also affects the shape of the initial sound velocity profiles — the characteristic minima and maxima in the profiles, which are important for the propagation of sound, were smoothed. This would prohibit a successful forecast of sound velocity structure, because the initial structure was already wrong. Therefore, during the course of the integration, the observed temperature and salinity profiles of data set A were assimilated into the model solution from 8 February 06:00h to 12 February 16:00h in 6-hour time

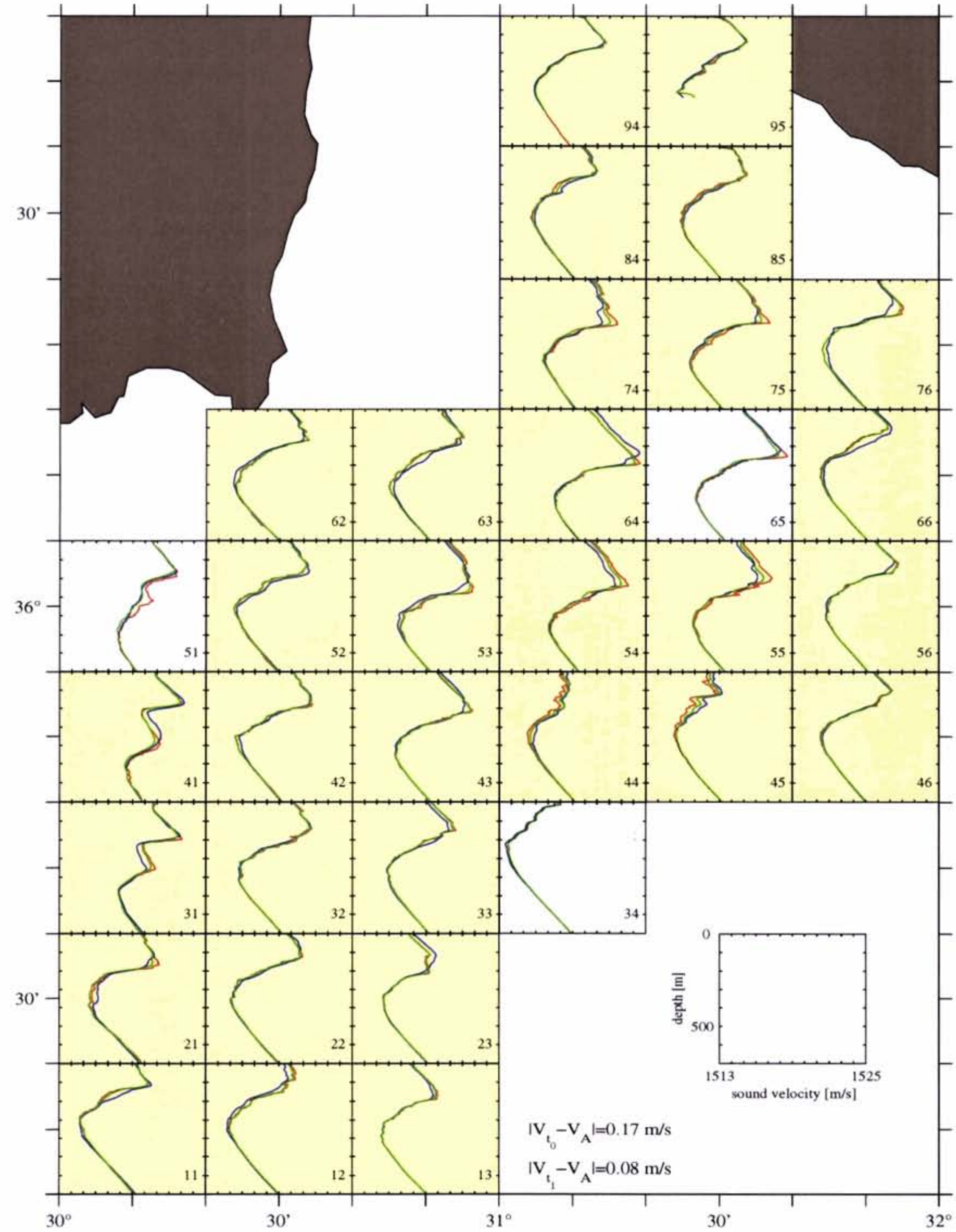

Figure 17 *Sound velocity profiles at positions of casts of subset A. Red: measured validation profiles of subset A. Blue: model initial profiles at $t = t_0$. Green: profiles assimilated into the model solution at time $t = t_1$ when the casts were taken. The centre of each subplot corresponds to the position of the profiles, numbers in the lower right corner serve for identification. Yellow axes back panels indicate that the assimilated profiles are closer to the validation profiles than the initial ones.*

intervals, but now using dynamically consistent values of Γ=20 km and Λ=30 km for the correlation scale and the zero-crossing scale, respectively. The temporal correlation scale was set to τ=12 hours. Hence, the same profiles, which were already used for model initialization, are serving now for keeping the model solution on track; in contrast to the initial setup, however, the small values for Γ, Λ and τ enable that the model sound velocity profiles at the positions of the CTD casts of data set A are matching more closely the measured profiles in space and in time, and an improvement of the quality of the forecast can be expected. This is illustrated by Figure 17, where the model initial sound velocity profiles $V_{t_0}(z)$ (blue curves), the assimilated profiles $V_{t_1}(z)$ (green) and the measured profiles $V_A(z)$ (red) are combined each in one graph, which is centred at the position of the respective CTD cast of subset A. In order to decide which profiles agree better with the red validation profiles, the mean differences $\Theta_{0,A} = \overline{|V_{t_0}(z) - V_A(z)|}$ between the blue and the red and $\Theta_{1,A} = \overline{|V_{t_1}(z) - V_A(z)|}$ between the green and the red were evaluated, where the overbar denotes averaging over all depth levels. The axes back panels of those subplots where $\Theta_{1,A} < \Theta_{0,A}$, are yellow, i. e. in 31 out of 34 locations the assimilation leads to more realistic profiles at the position of the observed casts. To be more quantitative, $\Theta_{0,A}$ and $\Theta_{1,A}$ were averaged over all 34 subplots yielding mean values of $\overline{\Theta_{0,A}} = 0.17$ m s^{-1} and $\overline{\Theta_{1,A}} = 0.08$ m s^{-1} . Thus the difference between initial and validation profiles is reduced by about 50% by assimilation.

7.3 Validation

In order to assess whether a meaningful forecast may be expected from the model, the observed changes of temperature and velocity at 200 m depth between leg 1/1 and leg 1/2 (Figures 16, 18) are compared with the respective model initial situation and the forecast of 12 February 18:00h. The most significant observed changes are

- (i) The Antalya Anticyclone changes size from elliptical to more circular.
- (ii) The centre of the Antalya Anticyclone is displaced to the southwest by about 20 km.
- (iii) The shape of the cyclonic eddy previously centred at about (31°20′E, 35°40′N) changed to a more elongated cyclonic feature with two cold centres.

Qualitatively, changes (i)–(iii) are also reproduced by the model, but with respect to the following items the forecast is different from the leg 1/2 observations:

- (I) The high velocity band of the Antalya Anticyclone is narrower.
- (II) The Anaximander Anticyclone seems to separate from the coast.

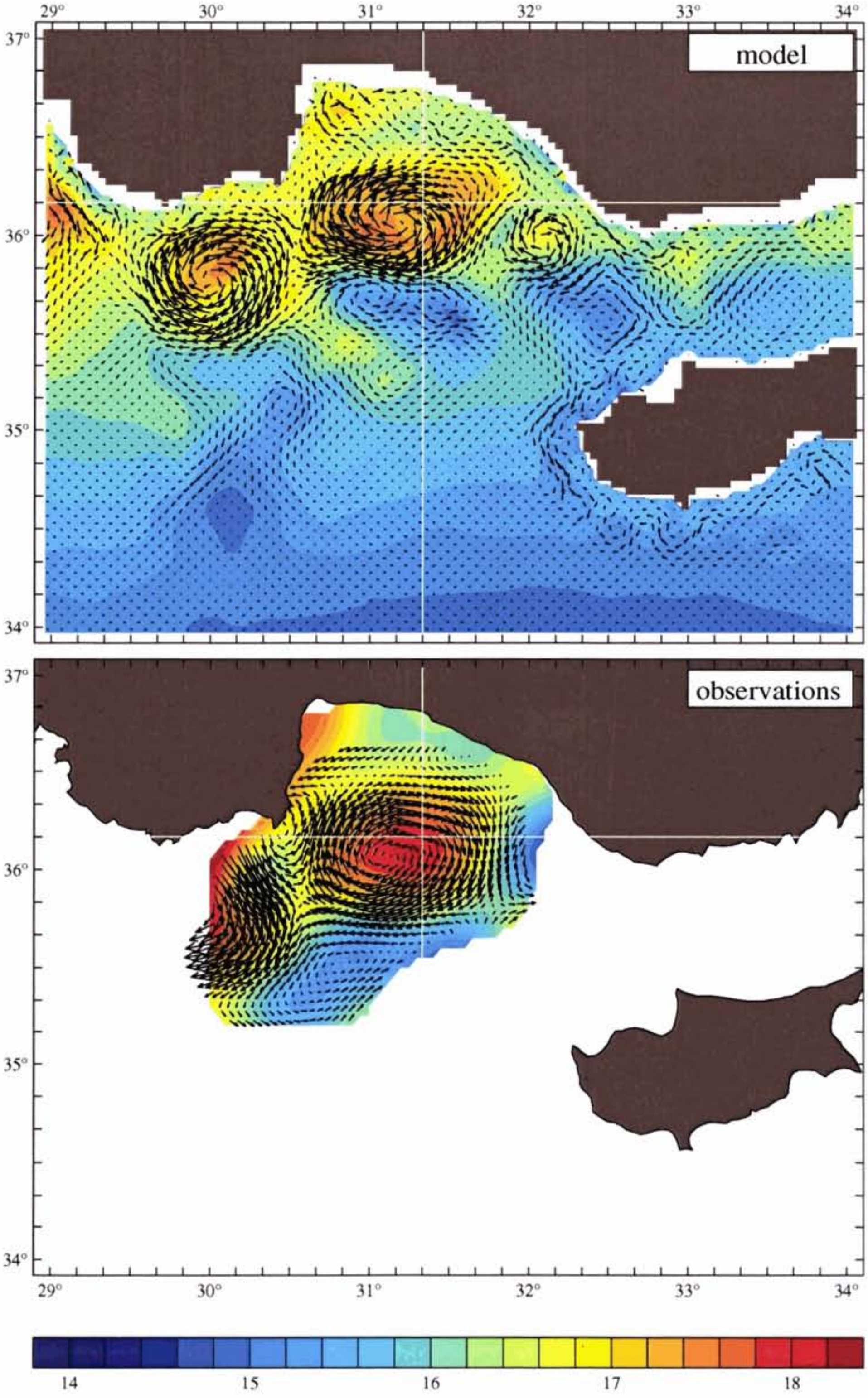

Figure 18 *Forecasted distributions of temperature [°C] and horizontal velocity at 200 m depth for 12 February 18:00h and corresponding observations from leg 1/2. The white crosshair is at the same position as in Figure 16.*

(III) The elongated cyclonic feature (iii) extends less far to the west and its meridional extent is less.

(IV) A small anticyclone has developed close to the coast east of the Antalya Anticyclone.

(V) There is evidence for cooling in the Antalya Anticyclone and along the coast.

From items (I)–(IV) it is highly probable that the parameters controlling the horizontal diffusion of either temperature, salinity, momentum, or vorticity were selected not adequately. Items (II) and (IV) may be due to wrong settings of coefficients controlling coastal and bottom friction, and a too large vertical diffusion coefficient might have lead to (V). Generally, it would be possible to find a suitable combination of these parameters, which would lead to a better match of the forecast with the observations, however, this would require a large number of additional model runs. It should also be mentioned that some of the misfits between forecast and validation are certainly caused by lack of observational data for model initialization. More data in the south and west would have yielded a dynamically more correct representation of the Asia Minor Current front and the Anaximander Anticyclone in the model, and in consequence of that more realistic model dynamics.

Three different sets of sound velocity profiles are displayd in Figure 19. The red profiles are the validation profiles from data subset B, and the green ones are the forecasted profiles at the respective position. As the model produces an output only every 6 hours, the forecasted profiles are interpolated in time to the instant $t = t_2$ when the validation casts were taken. Finally, the blue profiles are those from data subset A, which have been assimilated into the model solution during the startup phase at $t = t_1$. They are identical with the green ones in Figure 17. A first test for assessment of the quality of the forecast is to check whether the forecasted profiles are closer to the validation profiles than the assimilated ones. Therefore, the mean differences $\Theta_{A,B} = \overline{|V_A(z) - V_B(z)|}$ between the blue and the red and $\Theta_{2,B} = \overline{|V_{t_2}(z) - V_B(z)|}$ between the green and the red were evaluated and yellow axes back panels indicate those subplots where $\Theta_{2,B} < \Theta_{A,B}$. This condition is satisfied in 18 out of 34 subplots, hence the model prediction is slightly better than making the assumption that no change occurred during the forecast period. This is also confirmed by taking the mean of $\Theta_{A,B}$ and $\Theta_{2,B}$ over all subplots yielding $\overline{\Theta_{A,B}} = 0.46$ m s^{-1} and $\overline{\Theta_{2,B}} = 0.44$ m s^{-1}.

An additional quality test is to check whether the model predicts correctly the *tendency* of temporal sound velocity changes. Accordingly, Figure 20 compares $\Theta_{2,A}(z) = V_{t_2}(z) - V_A(z)$, which is the difference curve between the forecasted profiles at $t = t_2$ and those assimilated from data subset A at $t = t_1$, and the difference profile $\Theta_{B,A}(z) = V_B(z) - V_A(z)$, which is the corresponding validation quantity between the casts of data subsets B and A. The correlation coefficient

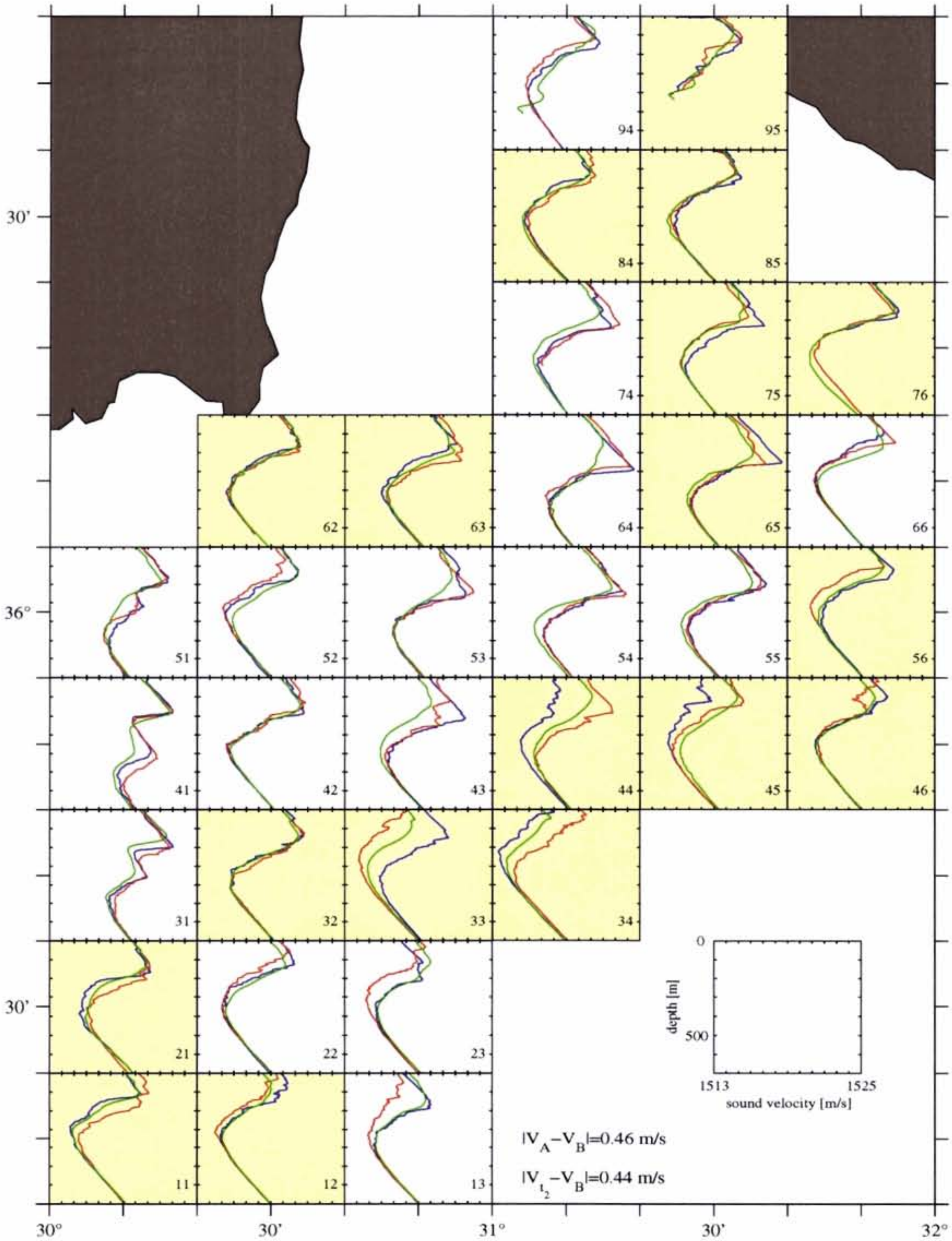

Figure 19 *Sound velocity profiles at positions of subset B casts. Red: validation profiles of subset B. Blue: initial profiles of subset A. Green: forecasted profiles at $t = t_2$ when the validation casts were taken. The centre position of each subplot corresponds to the positions of the profiles, numbers in the lower right corner of the subplots serve for identification. Yellow axes back panels indicate that the forecasted profiles are closer to the validation profiles than the initial ones.*

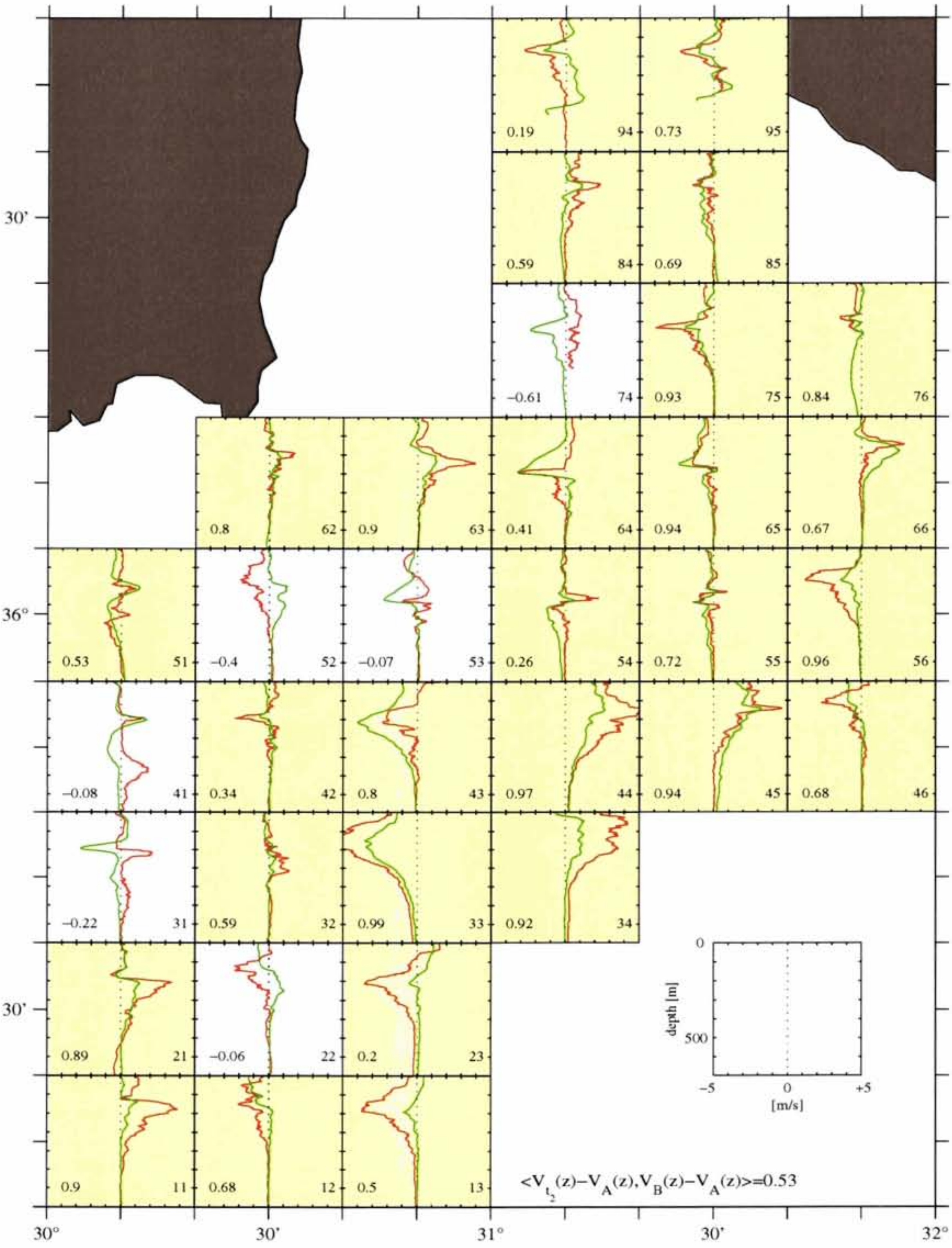

Figure 20 *Temporal changes of sound velocity. Red: difference between profiles of data subsets B and A. Green: difference between corresponding model profiles. The centre of each subplot corresponds to the position of profiles, numbers in the lower right serve for identification. The number in the lower left is the correlation coefficient between the difference profiles. Yellow axes back panels indicate positive correlation.*

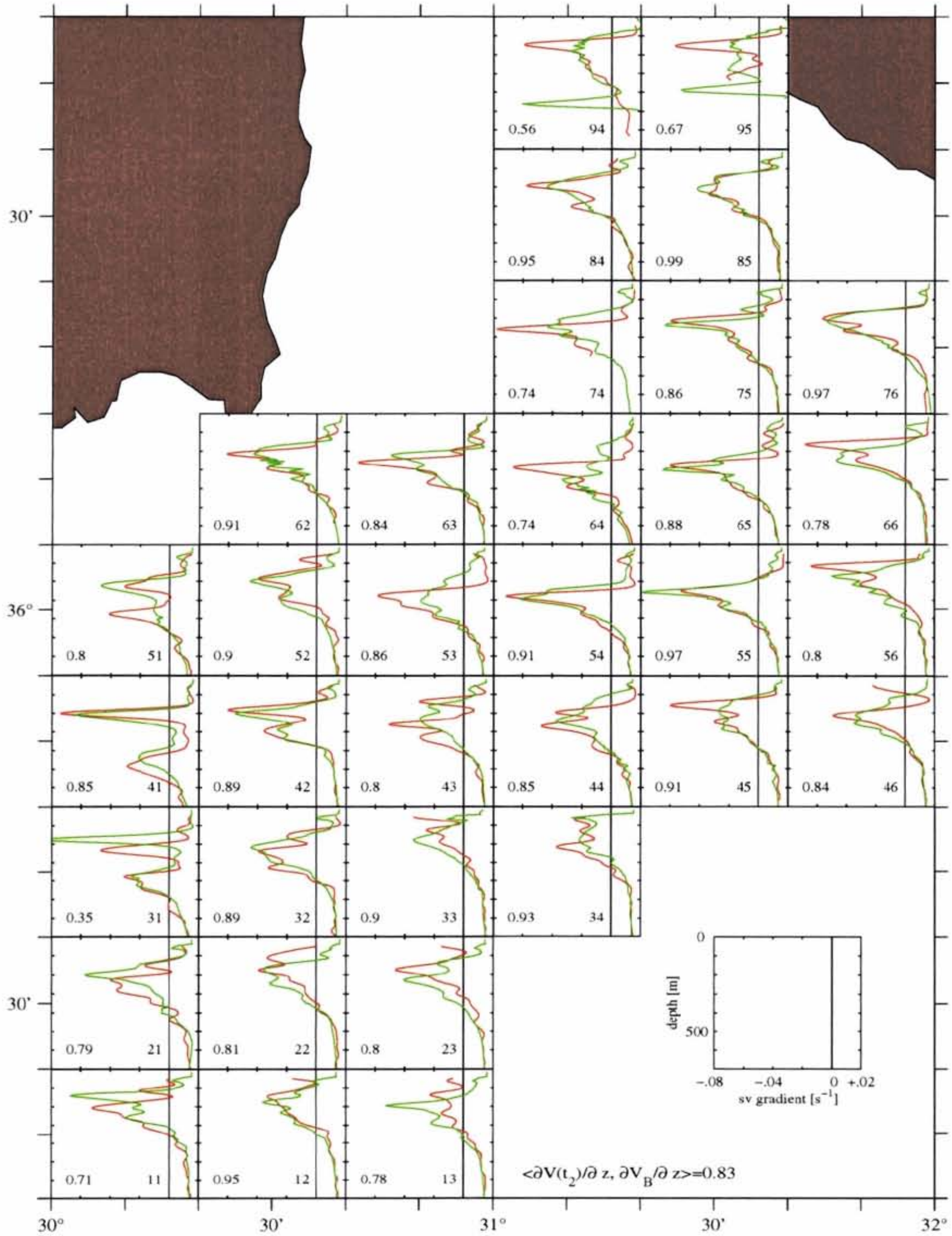

Figure 21 *Vertical gradient of sound velocity from forecasted (green) and validation profiles (red) of data subset B. The centre of each subplot corresponds to the position of profiles, numbers in the lower right serve for identification. The number in the lower left is the correlation coefficient between the green and red profiles.*

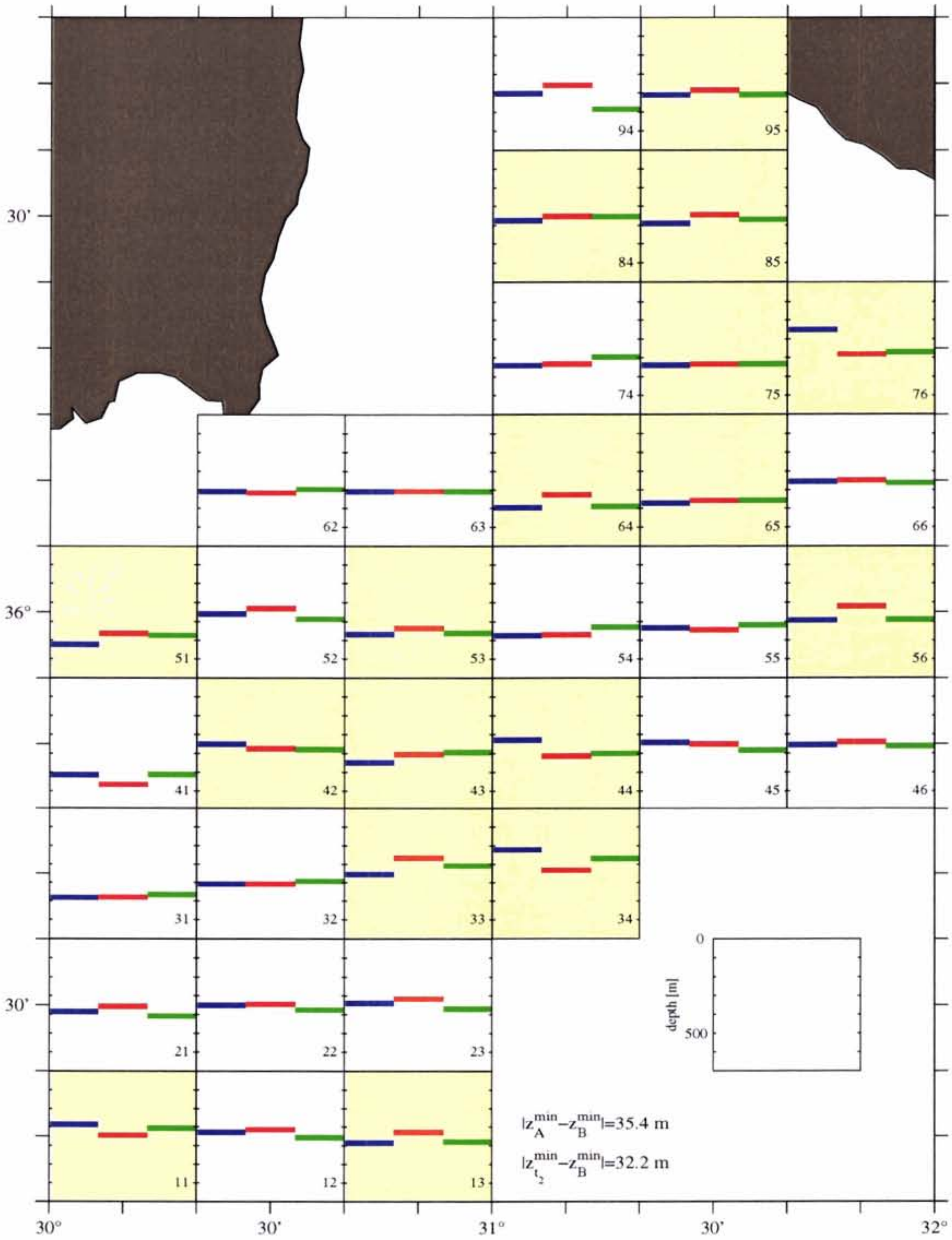

Figure 22 *Depth of sound velocity minimum. Red: validation depth from data subset B. Blue: initial depth from data subset A. Green: forecasted depth at* $t = t_2$ *when the validation casts were taken. The centre position of each subplot corresponds to the positions of the profiles, numbers in the lower right corner of the subplots serve for identification. Yellow axes back panels indicate that the forecasted depth is closer to the validation depth than the depth from the initial profiles.*

between both curves is written in the lower left corner of each subplot, and yellow axes back panels indicate subplots where the correlation is positive. Hence, in 28 out of 34 locations the positive correlation indicates that the tendency of the predicted sound velocity change is similar to that occurring in nature. This is also expressed by the mean correlation taken over all 34 subplots being 0.53.

The propagation of sound is strongly controlled by refraction, which depends solely on the sound velocity gradient. As the vertical gradients are several orders of magnitude larger than the horizontal, it is essential for a good forecast to predict them correctly. The forecasted vertical gradients $\partial V_{t_2}/\partial z$ and those from the validation profiles $\partial V_B/\partial z$ are compared in Figure 21. To make both quantities comparable, the gradients from the original casts were filtered by applying a 25-point moving average four times in order to remove high-wavenumber fluctuations due to the higher vertical resolution (1 m). Figure 21 shows that the forecasted and the filtered measured gradients are of the same order of magnitude and well correlated. At 26 out of 34 locations the correlation is higher than 0.8, and the mean over all subplots is 0.83. This means that at least at low frequencies, where the wavelength of sound waves is of the same order as the model vertical resolution, the sound rays would follow similar paths in the forecasted and the measured environment. For comparison, the correlation between the gradient profiles from data subsets A and B is 0.81. Thus, the forecast product is again better than the no-change assumption.

A relevant parameter for sound propagation is the depth of the sound velocity minimum, z^{min}, which is the depth of the axis of the main sound channel. A comparison of $z_{t_2}^{min}$, z_A^{min} and z_B^{min}, i. e. the minimum depths from the model forecast, the initial data subset A, and the validation data subset B, is displayed in Figure 22 by coloured bars. Yellow axes back panels indicate subplots where $\Theta_{2,B} = |z_{t_2}^{min} - z_B^{min}| < \Theta_{A,B} = |z_A^{min} - z_B^{min}|$, which is true in 17 out of 34 cases. However, it should be noted that in most situations where this condition is not satisfied, the difference between the forecasted minimum depth and the validation depth is rather small. Averaged over all 34 subplots, $\overline{\Theta_{A,B}}=35.4$ and $\overline{\Theta_{2,B}}=32.2$, thus in the mean, the predicted depth is better than the depth from the no-change assumption.

8
Conclusions

In the present study it has been shown that ocean modeling is a valuable tool for the assessment and prediction of sound velocity structure in the ocean. The Harvard Ocean Prediction System (HOPS) was applied to a unique data set enabling the validation of model nowcasts and forecasts.

The nowcast experiment has shown that horizontal interpolation of sound velocity by objective analysis is superior to a method that takes account only of the neighboured sound velocity profiles by means of inverse distance weighting. The superiority of objective analysis is due to the fact that the distance of contributing profiles is weighted by a correlation function, the structure of which is determined by the Rossby radius as a natural e-foding scale for dynamical processes in the ocean. For future sea trials it is therefore recommended to determine the Rossby radius for the geographical area first, and then to adjust the survey pattern in a way that the horizontal resolution is close to the Rossby radius. This prohibits undersampling and oversampling as well.

The forecast experiment has demonstrated the capability of HOPS to achieve a meaningful prediction of sound velocity structure. For a forecast period of a few days, it has been verified that the predicted evolution of sound velocity profiles is highly correlated with the measured evolution from the validation data. It has further been shown that the predicted profiles, their vertical gradients, and the depth of the main sound channel axis provide a better match with the validation data than making the assumption that no change has occurred during the forecast period. However, for a successful prediction it is necessary to run the model with high vertical resolution in order to resolve minima and maxima of sound velocity adequately. Special care has to be taken during the startup phase of the model; the temperature and salinity profiles utilized for model initialization should reflect the real sound velocity profiles as close as possible and smoothing must be minimized.

For the model experiments, HOPS was applied to a data set of an oceanic region exhibiting high spatial and temporal variability due to mesoscale eddies and rapidly propagating frontal meanders. Although the resolution of the observational data was sufficient in space and time, the HOPS nowcasts and forecasts certainly would have been improved if the survey area would have been extended to the south and west. This would have enabled a better sampling of the Asia Minor Current front and the Anaximander Anticyclone and consequently a dynamically more correct model initialization. Therefore, it is recommended for future experiments that the observational data serving as input for nowcasts and model initialization should cover a horizontal area which is at least a few Rossby radii wider than the area for which nowcasts and forecasts are requested.

9

Glossary

a = weighting coefficient
BNDO = Bureau National des donnees oceanographiques,
Brest, France
C = correlation function
CTD = Conductivity-Temperature-Depth probe
D_S = diffusion of salinity
D_T = diffusion of heat
d = distance
div = divergence
E = error variance
F = arbitrary function
$\mathbf{F}$ = force
$\mathbf{F}_c$ = Coriolis force
$\mathbf{F}_f$ = friction force
$\mathbf{F}_g$ = gravitational force
$\mathbf{F}_p$ = pressure gradient force
$\mathbf{F}_t$ = tidal force
f = Coriolis parameter
GDEM = General Digital Environmental Model
g = gravitational acceleration
H = layer thickness
HOPS = Harvard Ocean Prediction System
I = number of grid cells in x-direction
i = index
J = number of grid cells in y-direction
j = index
K = number of grid cells (layers) in z-direction
k = index
l = index
M = mass
MODB = Mediterranean Ocean Data Base
MOODS = Master Oceanographic Data Set
m = index
NAVOCEANO = Naval Oceanographic Office,
Stennis Space Center, Mississippi, USA

NODC = National Oceanographic Data Center,
Washington D. C., USA
n = time level
p = pressure
P_T = pressure work
R = remainder of Taylor series
R_D = Rossby radius
R_T = absorption of solar radiation
r = index
S = salinity
s = index
T = temperature
$\mathbf{U}$ = velocity vector
UTC = Coordinated Universal Time
t = time
u = eastward velocity component
V = sound velocity
v = northward velocity component
w = vertical velocity component
x = eastward coordinate
X = arbitrary physical property
XBT = Expendable Bathythermograph
XCTD = Expendable Conductivity-Temperature-Depth probe
XSV = Expendable Sound Velocity probe
y = northward coordinate
z = vertical coordinate
α = error variance correlation matrix
β = correlation matrix
Γ = e-folding scale of correlation function
Δ = finite interval
δ = identity matrix
Θ = mean difference
ϑ = difference
Λ = zero-crossing scale of correlation function
λ = geographical longitude
ξ = arbitrary independent variable
ϱ = density
τ = temporal correlation scale
φ = geographical latitude
Ω = angular velocity of the earth

Acknowledgements

The oceanographic data for this study were collected by *NRV Alliance* and *TCG Çubuklu* during the POYRAZ97 survey. The readiness and skill of the crews of boths vessels and the support of the Turkish Navy Department of Navigation, Hydrography and Oceanography are greatly acknowledged. The MODB-MED2 climatology of the Mediterranean Sea was provided by the MODB (Mediterranean Ocean Data Base) project, which is funded by the European Commission as part of the MAST-II program under contract EUR-MAS2-CT93-0075-BE. The GDEM climatology was obtained from the Naval Oceanographic Office, Stennis Space Center, Mississippi.

References

[1] A. E. Gill. *Atmosphere–Ocean Dynamics.* Academic Press, New York, 1982. 662 pp.

[2] S. Pond and G. L. Pickard. *Introductory Physical Oceanography.* Pergamon, Oxford, 1983. 329 pp.

[3] J. Pedlosky. *Geophysical Fluid Dynamics.* Springer Verlag, New York, 1987. 710 pp.

[4] H.-G. Ramming. *Numerical Modelling of Marine Hydrodynamics - Applications to Dynamical Physical Processes*, volume 26 of *Elsevier Oceanography Series.* Elsevier, 1980. 368 pp.

[5] F. Mesinger and A. Arakawa. *Numerical Methods Used in Atmospheric Models I.* Number 17 in GARP Publication Series. World Meteorological Organization, 1976. 66pp.

[6] P. Malonotte-Rizzoli. *Modern Approaches to Data Assimilation in Ocean Modeling*, volume 61 of *Elsevier Oceanography Series.* Elsevier, Amsterdam, 1996. 455 pp.

[7] R. Onken. Oceanographic conditions in the Antalya Basin in winter. SACLANTCEN Report SR–299, SACLANT Undersea Research Centre, La Spezia, Italy, 1998 (in press).

[8] R. Onken and H. Yüce. Winter circulation and convection in the Antalya Basin (Eastern Mediterranean). *J. Phys. Oceanogr.*, 1999 (submitted).

[9] C. J. Lozano, P. Haley, H. Arango, Q. Sloan, and A. R. Robinson. Harvard coastal/deep water primitive equation model. Unpublished, 1994.

[10] National Geographic Data Centre. ETOPO5 — 5-minute gridded elevations/ bathymetry for the world. In *Global Relief CD-ROM.* National Geographic Data Centre, Boulder, Colorado, 1993.

[11] R. L. Haney. On the pressure gradient force over steep topography in sigma coordinate ocean models. *J. Phys. Oceanogr.*, 21(4):610–619, 1991.

[12] W. J. Teague, M. J. Carron, and P. J. Hogan. A comparison between the Generalized Digital Environmental Model and Levitus climatologies. *J. Geophys. Res.*, 95(C5), 1990.

[13] P. Brasseur, J. M. Beckers, J. M. Brankart, and R. Schoenauen. Seasonal temperature and salinity fields in the Mediterranean Sea: Climatological analyses of a historical data set. *Deep-Sea Res.*, 43(2):159–192, 1996.

[14] F. P. Bretherton, R. E. Davis, and C. B Fandry. A technique for objective analysis and design of oceanographic experiments applied to MODE-73. *Deep-Sea Res.*, 23(7):559–582, 1976.

[15] E. Özsoy, A. Hecht, and Ü. Ünlüata. Circulation and hydrography of the Levantine Basin. Results of POEM coordinated experiments 1985–1986. *Progr. Oceanogr.*, 22:125–170, 1989.

[16] E. Özsoy, A. Hecht, Ü. Ünlüata, S. Brenner, T. Oğuz, J. Bishop, M. A. Latif, and Z. Rozentraub. A review of the Levantine Basin circulation and its variability during 1985–1988. *Dyn. Atm. Oceans*, 15:421–456, 1991.

[13] P. Brasseur, J. M. Beckers, J. M. Brankart, and R. Schoenauen. Seasonal temperature and salinity fields in the Mediterranean Sea: Climatological analyses of a historical data set. *Deep-Sea Res.*, 43(2):159–192, 1996.

[14] F. P. Bretherton, R. E. Davis, and C. B Fandry. A technique for objective analysis and design of oceanographic experiments applied to MODE-73. *Deep-Sea Res.*, 23(7):559–582, 1976.

[15] E. Özsoy, A. Hecht, and Ü. Ünlüata. Circulation and hydrography of the Levantine Basin. Results of POEM coordinated experiments 1985–1986. *Progr. Oceanogr.*, 22:125–170, 1989.

[16] E. Özsoy, A. Hecht, Ü. Ünlüata, S. Brenner, T. Oğuz, J. Bishop, M. A. Latif, and Z. Rozentraub. A review of the Levantine Basin circulation and its variability during 1985–1988. *Dyn. Atm. Oceans*, 15:421–456, 1991.

Report no. changed (Mar 2006): SR-292-UU

Document Data Sheet

Security Classification		*Project No.* 022-3
Document Serial No. SR-292	*Date of Issue* April 1999	*Total Pages* 60 pp.

Author(s)

Onken, R.

Title

Nowcasting and forecasting of sound velocity structure by ocean modeling

Abstract

The Harvard Ocean Prediction System (HOPS) is applied to an observed oceanographic data set in order to demonstrate that a dynamical ocean model is able to provide meaningful nowcasts and forecasts of the three-dimensional distribution of sound velocity. The high resolution observational data collected in February 1997 in the Antalya Basin (Eastern Mediterranean Sea) are serving for initialization of the model and for validation of the model results.

For assessing the nowcast capability, HOPS is initialized by a subset of observational data at half the horizontal resolution of the original sampling scheme. The sound velocity field is obtained by objective analysis, which performs a linear estimate of sound velocity at any location in three-dimensional space. The power of this method is due to the fact that the contribution of every single observation is weighted by a spatial and temporal correlation function, the spatial structure of which is determined by the Rossby radius as a natural e-folding scale for dynamical processes in the ocean. The modelled sound velocity distribution is validated by comparison with the full resolution observed distribution at the respective locations, and it is shown that the objectively analyzed sound velocity matches the observations better than the sound velocity distribution obtained by a classical interpolation scheme with inverse distance weighting.

For the forecast experiment, the observational data set is separated in two subsets which occupy the same positions but are different in time. HOPS is initialized with the earlier data set and integrated in time until the end of the survey. By comparing the forecasted and observed sound velocity during the course of the integration, it is verified that the predicted profiles, their vertical gradients, and the depth of the main sound channel axis provide a better match with the validation data than making the assumption that no change has occurred during the forecast period.

Keywords

Eastern Mediterranean - sound velocity - nowcast - ocean modeling

Issuing Organization

North Atlantic Treaty Organization
SACLANT Undersea Research Centre
Viale San Bartolomeo 400, 19138 La Spezia, Italy

[From N. America: SACLANTCEN
(New York) APO AE 09613]

Tel: +39 0187 527 361
Fax:+39 0187 524 600

E-mail: library@saclantc.nato.int

Report no. changed (Mar 2006): SR-292-UU

Initial Distribution for Unclassified SR-292

Ministries of Defence

DND Canada	10
CHOD Denmark	8
DGA France	8
MOD Germany	15
HNDGS Greece	12
MARISTAT Italy	9
MOD (Navy) Netherlands	12
NDRE Norway	10
MOD Portugal	5
MDN Spain	2
TDKK and DNHO Turkey	5
MOD UK	20
ONR USA	34

NATO Commands and Agencies

NAMILCOM	2
SACLANT	3
CINCEASTLANT/ COMNAVNORTHWEST	1
CINCIBERLANT	1
CINCWESTLANT	1
COMASWSTRIKFOR	1
COMSTRIKFLTANT	1
COMSUBACLANT	1
SACLANTREPEUR	1
SACEUR	2
CINCNORTHWEST	1
CINCSOUTH	1
COMEDCENT	1
COMMARAIRMED	1
COMNAVSOUTH	1
COMSTRIKFORSOUTH	1
COMSUBMED	1
NC3A	1
PAT	1

Scientific Committee of National Representatives

SCNR Belgium	1
SCNR Canada	1
SCNR Denmark	1
SCNR Germany	1
SCNR Greece	1
SCNR Italy	1
SCNR Netherlands	2
SCNR Norway	1
SCNR Portugal	1
SCNR Spain	1
SCNR Turkey	1
SCNR UK	1
SCNR USA	2
French Delegate	1
SECGEN Rep. SCNR	1
NAMILCOM Rep. SCNR	1

National Liaison Officers

NLO Canada	1
NLO Denmark	1
NLO Germany	1
NLO Italy	1
NLO Netherlands	1
NLO Spain	1
NLO UK	1
NLO USA	1

Sub-total	199
SACLANTCEN	30
Total	229